Development/Plasticity/Repair

Maturation Dynamics of the Axon Initial Segment (AIS) of Newborn Dentate Granule Cells in Young Adult C57BL/6J Mice

Marta Bolós,[1,2] **Julia Terreros-Roncal,**[1,2,3] **Juan R. Perea,**[1,2] **Noemí Pallas-Bazarra,**[1,2] **Jésus Ávila,**[1,2] **and María Llorens-Martín**[1,2,3]

[1]Department of Molecular Neuropathology, Centro de Biología Molecular Severo Ochoa (CBMSO, Consejo Superior de Investigaciones Científicas-Universidad Autónoma de Madrid), Madrid 28049, Spain, [2]Center for Networked Biomedical Research on Neurodegenerative diseases, Madrid 28031, Spain, and [3]Department of Molecular Biology, Faculty of Sciences, Universidad Autónoma de Madrid, Madrid 28049, Spain

Newborn dentate granule cells (DGCs) are generated in the hippocampal dentate gyrus (DG) of rodents through a process called adult hippocampal neurogenesis, which is subjected to tight intrinsic and extrinsic regulation. The use of retroviruses encoding fluorescent proteins has allowed the characterization of the maturation dynamics of newborn DGCs, including their morphological development and the establishment and maturation of their afferent and efferent synaptic connections. However, the study of a crucial cellular compartment of these cells, namely, the axon initial segment (AIS), has remained unexplored to date. The AIS is not only the site of action potential initiation, but it also has a unique molecular identity that makes it one of the master regulators of neural plasticity and excitability. Here we examined the dynamics of AIS formation in newborn DGCs of young female adult C57BL/6J mice *in vivo*. Our data reveal notable changes in AIS length and thickness throughout cell maturation under physiological conditions and show that the most remarkable structural changes coincide with periods of intense morphological and functional remodeling. Moreover, we demonstrate that AIS development can be modulated extrinsically by both neuroprotective (environmental enrichment) and detrimental (lipopolysaccharide from *Escherichia coli*) stimuli.

Key words: **adult neurogenesis; axon initial segment; environmental enrichment; hippocampus; neuroinflammation; structural plasticity**

Significance Statement

The hippocampal dentate gyrus (DG) of rodents generates newborn dentate granule cells (DGCs) throughout life. This process, named adult hippocampal neurogenesis, confers a unique degree of plasticity to the hippocampal circuit, and it is crucial for learning and memory. Here we studied, for the first time, the formation of a key cellular compartment of newborn DGCs, namely, the axon initial segment (AIS) *in vivo*. Our data reveal remarkable AIS structural remodeling throughout the maturation of these cells under physiological conditions. Moreover, AIS development can be modulated extrinsically by both neuroprotective (environmental enrichment) and detrimental (lipopolysaccharide from *Escherichia coli*) stimuli.

Introduction

Dentate granule cells (DGCs) are generated in the dentate gyrus (DG) of rodents throughout life (Altman and Das, 1965). This process, named adult hippocampal neurogenesis (AHN), encompasses several stages of maturation that lead to the synaptic integration of newborn DGCs into the hippocampal trisynaptic circuit (Zhao et al., 2006; Toni et al., 2008). Genetically engineered retroviruses encoding fluorescent proteins have greatly expanded our knowledge of AHN (Enikolopov et al., 2015) because they allow the visualization of the whole morphology and synaptic structures of individual newborn DGCs (van Praag et al., 2002; Zhao et al., 2006; Llorens-Martín et al., 2015a). However, a

Received Sept. 1, 2018; revised Dec. 27, 2018; accepted Jan. 4, 2019.

Author contributions: M.B., J.T.-R., J.R.P., N.P.-B., J.Á., and M.L.-M. edited the paper; M.L.-M. wrote the first draft of the paper; M.L.-M. designed research; M.B., J.T.-R., J.R.P., N.P.-B., and M.L.-M. performed research; J.Á. contributed unpublished reagents/analytic tools; M.B., J.T.-R., J.R.P., N.P.-B., and M.L.-M. analyzed data; M.L.-M. wrote the paper.

This work was supported by the Spanish Ministry of Economy and Competitiveness SAF-2017-82185-R and RYC-2015-171899 to M.L.-M. and SAF-2014-53040-P to J.Á., Centro de Investigación Biomédica en Red sobre Enfermedades Neurodegenerativas to J.Á., Alzheimer's Association 2015-NIRG-340709 and AARG-17-528125 to M.L.-M., Association for Frontotemporal Degeneration 2016 Basic Science Pilot Grant Award to M.L.-M., and Fundación Ramón Areces and Banco de Santander to the Centro de Biología Molecular Severo Ochoa Institutional Grants.

The authors declare no competing financial interests.

Correspondence should be addressed to María Llorens-Martín at m.llorens@csic.es.

https://doi.org/10.1523/JNEUROSCI.2253-18.2019

 0270-6474/19/391605-16$15.00/0

crucial subcellular compartment, namely, the axon initial segment (AIS), has been systematically overlooked in the study of the functional maturation of these cells *in vivo*.

The AIS was first described by Conradi (1966) and Palay et al. (1968) as an independent cellular compartment located between the axonal hillock and the distal axon. The AIS serves not only as the site for action potential (AP) initiation (Colbert and Johnston, 1996; Palmer and Stuart, 2006; Hu et al., 2009; Grubb et al., 2011) but also as a cell polarity gatekeeper by maintaining the electric and chemical isolation of somatodendritic and axonal compartments (Dotti and Simons, 1990; Song et al., 2009; Watanabe et al., 2012; Edwards et al., 2013; Jones and Svitkina, 2016). The AIS has a unique molecular identity, which includes the presence of a remarkably high number of voltage-gated ion channels (Koontz, 1993; Colbert and Johnston, 1996; Kole et al., 2007; Bender and Trussell, 2009), a specialized extracellular matrix (Hedstrom et al., 2007), a tightly regulated and differential innervation (Somogyi, 1979; Christie and De Blas, 2003; Wang et al., 2014; Saha et al., 2017), and a variety of structural, cytoskeletal, and adaptor proteins (Leterrier, 2016). Among the latter, the scaffold protein Ankyrin G makes a crucial contribution to AIS assembly and maintenance (Leterrier et al., 2017).

A series of elegant studies have brought to light the extraordinary degree of structural and functional complexity exhibited by this structure (Rasband, 2010; Kole and Stuart, 2012; Jones and Svitkina, 2016). Indeed, remarkable structural remodeling occurs in the AIS both during neural development and in response to a variety of insults of distinct nature (Conradi and Ronnevi, 1977; Xu and Shrager, 2005; Schafer et al., 2009; Tapia et al., 2010; Clark et al., 2016, 2017; Schlüter et al., 2017; Leterrier, 2018).

Here we provide the first characterization of the temporal course of the formation and maturational dynamics of the AIS of newborn DGCs under physiological conditions, as well as in response to both neuroprotective (environmental enrichment [EE]) and detrimental (neuroinflammation caused by the lipopolysaccharide [LPS] from *Escherichia coli*) stimuli.

Materials and Methods

Experimental design

Maturation dynamics of the AIS of newborn DGCs. To facilitate observation of the whole morphology of newborn DGCs, C57BL/6J mice received a stereotaxic injection of a retrovirus that encodes Venus fluorescent protein (Gomez-Nicola et al., 2014). After a range of postinjection intervals, the animals were sacrificed. A schematic experimental design is shown in Figure 1. The tissues were then processed, and labeled DGCs were analyzed in terms of morphology: total dendritic length, Sholl's analysis, number of dendritic spines, and area of their axonal terminals (mossy fiber terminals; MFTs). In addition, the AIS of these cells was studied. Five mice were used for each time point examined.

External regulation of AIS formation in newborn DGCs. To study the extrinsic regulation of AIS formation in newborn DGCs, we followed two strategies. On the one hand, a group of mice was subjected to a period of EE, a paradigm that markedly increases hippocampal plasticity and the maturation of this neuronal population (Alvarez et al., 2016), or to control housing (CH) conditions (see Fig. 4*A*). On the other hand, to test whether the formation of the AIS in newborn DGCs is impaired by a deleterious stimulus, two additional groups of mice were implanted with subcutaneous pumps filled with either LPS or PBS (see Fig. 6*A*). Systemic administration of LPS causes hippocampal neuroinflammation and impairs newborn DGC maturation (Ekdahl et al., 2003; Monje et al., 2003; Llorens-Martín et al., 2014). Five mice were used for each experimental condition.

All stereotaxic injections, tissue processing, cell counts, and morphometric determinations were performed by trained researchers blind to the experimental conditions.

Animals

Five-week-old C57BL/6J Ola Hsd female mice were obtained from Envigo Laboratories. They were maintained undisturbed for 2 weeks in a specific pathogen-free colony facility at Centro de Biología Molecular Severo Ochoa before being subjected to experimental manipulations. At the moment of stereotaxic injections, all mice were 7 weeks old. They were housed in ventilated racks in a pathogen-free colony facility at the Centro de Biología Molecular Severo Ochoa, in accordance with European Community Guidelines (directive 86/609/EEC), and handled following European and local animal care protocols. Two or three mice were housed per cage. Five mice were used for each experimental condition and time point examined. Animal experiments received the approval of the Centro de Biología Molecular Severo Ochoa Ethics Committee (AEEC-CBMSO-23/172) and the National Ethics Committee (PROEX 205/15).

Retroviral stock preparation

We used a retroviral stock encoding for Venus fluorescent protein on an RSF91 backbone (Schambach et al., 2006; Gomez-Nicola et al., 2014). The plasmids used to produce the virus were kindly provided by Prof. Miyawaki (RIKEN Brain Science Institute), Dr. Riecken (University Medical Center Hamburg-Eppendorf), and Dr. Gage (Salk Institute). Retroviral stocks were concentrated to working titers of 1×10^7 to 1×10^8 pfu/ml by ultracentrifugation (Zhao et al., 2006). Because the retroviruses used are engineered to be replication-incompetent, only cells dividing at the time of surgery are infected (Zhao et al., 2006). In the DG, these proliferative cells are almost totally restricted to newborn DGCs (Zhao et al., 2006).

Stereotaxic surgery

Mice were anesthetized with isoflurane and placed in a stereotaxic frame. Retroviruses were injected into the DG at the following coordinates (millimeters) relative to bregma in the anteroposterior, mediolateral, and dorsoventral axes ($-2.0, \pm 1.4, 2.2$). Next, 2 μl of Venus/pCS2 retrovirus was infused at a rate of 0.2 μl/min via a glass micropipette. To avoid any suction effect of the solution injected, micropipettes were kept in place at the site of injection for an additional 5 min interval before being slowly removed. Animals were sacrificed after various periods of time, following the experimental design shown in Figure 1.

EE

We used a previously described EE protocol (Llorens-Martín et al., 2010). One week after retroviral injections, mice assigned to EE were housed in a large transparent polycarbonate cage ($55 \times 33 \times 20$ cm, Plexx Ref. 13005) (10 mice per cage) for an additional week (see Fig. 4*A*). All enriched cages were equipped with various types of running wheels. The mice had free access to toys of different shapes, sizes, materials, and surface textures. Every other day, a set of 10–15 different toys and new bedding were placed in the cages to alter the environment (Llorens-Martín et al., 2010). To examine the external regulation of AIS formation, the EE protocol was applied between 1 and 2 weeks after stereotaxic injections. This period comprised the time point at which the AIS was first observed in newborn DGCs (10 d). Given that no ventilated racks adapted to the dimensions of the enriched cages were available, and to rule out any putative influence of environmental noise or odors on the parameters studied, an additional group of mice were housed in nonventilated standard cages during the same period of time and were used as CH animals. CH animals were housed in groups of 2 or 3 per cage, whereas animals subjected to EE were housed in groups of 10 per cage.

Treatment with LPS from E. coli

LPS was administered subcutaneously via Alzet osmotic pumps (Durect) following the experimental design described in Figure 7*A*. Mouse #1002 model osmotic pumps were used. To test the effects of an extrinsic modulator, which did not cause remarkable morphological changes on newborn DGCs, on AIS formation, we used a low dose of LPS continuously delivered for 2 weeks. This period of time comprised the time point at which the presence of an AIS was first observed on DGCs. To achieve continuous LPS delivery of 150 μg kg^{-1} per day for 2 consecutive weeks, pumps were filled with a solution of LPS (Sigma-Aldrich, from *E. coli*

055:B5) diluted in 0.1 M PBS. Moreover, to rule out any putative effect of osmotic pump implantation, an additional group of control animals received osmotic pumps filled with 0.1 M PBS. Osmotic pumps were implanted at the time of stereotaxic injections.

Sacrifice

Mice were fully anesthetized by an intraperitoneal injection of pentobarbital (EutaLender, 60 mg/kg) and transcardially perfused with 0.9% saline followed by 4% PFA in 0.1 N phosphate buffer. Given that the immunohistochemical detection of Ankyrin G requires weak fixation of tissue (Alshammari et al., 2016), brains were removed and postfixed for 20 min in the same fixative at 4°C. They were then washed three times in 0.1 N phosphate buffer and placed in a 10% sucrose/4% agarose matrix to increase the robustness of the tissue and allow vibratome sectioning.

Immunohistochemistry

Immediately after inclusion, coronal brain sections were obtained on a VT1200S vibratome (Leica Microsystems, 50 μm thick sections). For immunohistochemical analysis, series of brain slices were randomly made up of one section from every ninth. Slices were initially preincubated in phosphate buffer with 1% Triton X-100 and 1% BSA. Dual immunohistochemistry was then performed as described previously (Llorens-Martín et al., 2013), using the following primary antibodies: rabbit anti-GFP (which detects Venus and enhances the fluorescence intensity of its signal) (Thermo Fisher Scientific catalog #A-11122, RRID: AB_221569; 1:1000); guinea pig anti-cfos (Synaptic Systems catalog #226 004, RRID:AB_2619946; 1:500); rabbit anti-Iba1 (Wako catalog #019-19741, RRID:AB_839504; 1:500); rat anti-CD68 (Abcam catalog #53444, RRID:AB_869007; 1:500); chicken anti-GFP (Abcam catalog #ab13970, RRID:AB_300798); and mouse anti-Ankyrin G (University of California–Davis/National Institutes of Health NeuroMab Facility catalog #75-146, RRID:AB_10673030; 1:1000). To detect the binding of primary antibodies, Alexa-594 donkey anti-mouse (Invitrogen catalog #A-21203, RRID:AB_141633; 1:1000), Alexa-488 donkey anti-rabbit (Invitrogen catalog #A-21206, RRID:AB_141708; 1:1000), Alexa-555 donkey anti-rabbit (Thermo Fisher Scientific catalog #A-31572, RRID:AB_162543; 1:1000), Alexa-647 goat anti-guinea pig (Thermo Fisher Scientific catalog #A-21450, RRID:AB_2735091), Alexa-647 goat anti-rat (Invitrogen catalog #A-21247, RRID:AB_141778), and Alexa-488 goat anti-chicken (Invitrogen catalog #A-11039, RRID:AB_142924) secondary antibodies were used. All the sections were counterstained for 10 min with DAPI (Merck, 1:5000) to label nuclei.

Morphometric analysis of newborn DGCs

Fifty randomly selected newborn DGCs from each experimental group and time point were reconstructed under a Nikon A1R confocal microscope (25× oil-immersion objective). Confocal stacks of images were obtained (z axis interval: 2 μm), and Z projections were analyzed to determine total dendritic length and dendritic arbor branching (Sholl's analysis). All cells were traced using *NeuronJ* plugin for Fiji software. Sholl's analysis was performed using the plugin *ShollAnalysis* for Fiji software. (Llorens-Martín et al., 2013; Pallas-Bazarra et al., 2017).

Potential changes in the position of the AIS could be attributable to somatic translocation processes (Murphy and Danzer, 2011). To rule out the occurrence of these phenomena, additional morphometric determinations were performed on the newborn DGCs of animals exposed to CH, EE, PBS, or LPS. In this regard, we first measured the length of the primary apical dendrite using Fiji software, as previously described (Llorens-Martín et al., 2014). Next, the percentage of cells showing basal dendrites was calculated (Llorens-Martín et al., 2013). Moreover, we measured the migration of individual newborn DGCs toward the granule cell layer (GCL) (Llorens-Martín et al., 2014). To this end, a line parallel to the hilar border of this structure, named the subgranular zone, was traced. The perpendicular distance between the center of the newborn DGC nucleus and this line was calculated using Fiji software. Finally, we calculated the distance between the axonal hillock and the first change of axonal trajectory toward the CA3 region, by tracing individual axons on z-projection images. This distance was calculated in Fiji software.

Morphometric analysis of the dendritic spines of newborn DGCs

Dendritic spines were studied in retrovirally labeled newborn DGCs of different ages. Confocal stacks of images were obtained in a Nikon A1R confocal microscope (63× oil-immersion objective; XY dimensions: 67.4 μm; z-axis interval: 0.2 μm). The dendritic length of each segment was measured on Z projections, and the number of dendritic spines was counted using *NeuronStudio* software (CNIC, Mount Sinai School of Medicine, 2007–2009) (Rodriguez et al., 2008). Before spine analysis, images were deconvoluted using Huygens Professional software (Scientific Volume Imaging). A minimum of 50 dendrites per experimental group and time point were examined. Dendritic fragments were automatically constructed using *NeuronStudio* software, and then individual seed points were rectified manually to more accurately trace the dendrite.

Analysis of cfos expression in DGCs

We first used the physical dissector method previously described (Llorens-Martín et al., 2006) to determine the total density of cells with cfos nuclear expression in the DG. To this end, 10 confocal stacks of images were obtained per animal in a LSM800 Zeiss confocal microscope (40× oil-immersion objective, Z interval: 1 μm). Next, the GCL was drawn, and the reference volume was calculated by multiplying the area of the GCL by the thickness of the Z stack. Next, the number of cfos$^+$ nuclei inside the reference volume was counted (Llorens-Martín et al., 2010), and this number was divided by this volume to obtain the density of cfos$^+$ cells (number of cells/mm^3).

Next, to specifically address the neuronal activation of newborn DGCs, we calculated the percentage of Venus$^+$ cells that showed a clear nuclear expression of cfos. At least 50 Venus$^+$ cells per animal were analyzed. Data were averaged per animal and represented in the graphs.

Area of MFTs of newborn DGCs

The area of individual Venus$^+$ MFTs was measured in the CA3 region. A minimum of 20 stacks of images per experimental condition and time point were obtained in a Nikon A1R confocal microscope (63× oil-immersion objective; XY dimensions: 100 μm; Z interval: 0.5 μm). Stacks were randomly obtained from the sections comprising the series. Z projections were obtained, and the area of each MFT was measured manually using Fiji software, as previously described (Toni et al., 2008; Pallas-Bazarra et al., 2016). A minimum of 400 MFTs per experimental condition and time point analyzed were measured.

Determination of the number of microglial cells and analysis of microglial activation

The number of Iba1$^+$ microglial cells in the GCL, molecular layer (ML), and hilus (H) was counted, as previously described (Llorens-Martín et al., 2014), following a similar methodology to that reported for cfos$^+$ cell counting. To this end, six confocal stacks of images were obtained per animal in a LSM800 Zeiss confocal microscope (40× oil-immersion objective, Z interval: 0.5 μm). The density of microglial cells present in each structure was averaged per animal and represented in the graphs.

To address the activation of microglial cells, we measured the expression of the microglial activation marker CD68, following a previously described methodology (Llorens-Martín et al., 2016). We first measured the CD68 fluorescence intensity on Z-projection images corresponding to each of the aforementioned subregions of the DG (see Fig. 7*L*). Moreover, colocalization between Iba1 and CD68 was analyzed by means of the *Just another colocalization plugin (JaCoP)* for Fiji software. M1 Mander's colocalization coefficient is shown in Figure 9*G*.

Morphometric analysis of the AIS of newborn DGCs

To analyze the morphometric parameters of the AIS of newborn DGCs of different ages, we measured the expression of the AIS marker Ankyrin G in the axons of retrovirally labeled cells. Before this quantification, close examination of the samples revealed the consistent absence of the AIS in immature cells, in which axonal identity has not yet been established (for a detailed description, see Discussion). Given that axonal projections show a regular thickness and are markedly thinner than dendrites, they were identified on the basis of morphological features (Zhao et al., 2006).

Analysis of the percentage of cells with a clearly identifiable axon and AIS. A minimum of 25 stacks of images per experimental condition and time

point were obtained in a Nikon A1R confocal microscope (63× oil-immersion objective; *Z* interval: 0.25 μm). More than 100 cells were examined per experimental condition and time point analyzed. The percentage of cells that exhibited a clearly identifiable axon was calculated. Moreover, the expression of Ankyrin G was verified at every point of the axonal trajectory by using the *Ortogonal Views* tool in Fiji software. The percentage of axons that showed Ankyrin G expression was calculated.

Analysis of AIS starting point, length, and thickness. A minimum of 100 cells per experimental condition were reconstructed under a Nikon A1R confocal microscope (63× oil-immersion objective; 2 × zoom; image XY dimensions: 200.33 μm; *Z* interval: 0.1 μm). The expression of Ankyrin G throughout axonal projections was confirmed in each plane of the *Z* stacks using the *Ortogonal Views* tool in Fiji software. To determine the AIS starting point, the axon was followed in the green channel, and the first point showing colocalization between GFP and Ankyrin G was identified. The distance between the axonal hillock and the starting point of Ankyrin G expression was then measured on *Z*-projection images using the freehand drawing tool of Fiji. For the sake of clarity, we named this parameter the AIS starting point. The distance between the AIS starting point and the ending point of Ankyrin G expression was measured using a similar methodology, and this parameter was denoted AIS length. Finally, the thickness of the AIS was measured on *Z* projections at three points, namely, the proximal (the closer to the soma), the medial, and the distal (the furthest) regions of this structure. The data on regional thickness are shown in the graphs. In addition, the average thickness of the AIS in the three aforementioned regions is also shown.

To further assure the reliability of the aforementioned measurements, the AIS starting point and length of 50 randomly selected 8-week-old newborn DGCs were independently analyzed by two researchers. Variation coefficients calculated by the relative interobserver variability method (Popović and Thomas, 2017) were ~5%.

Statistical analysis

Statistical analysis was performed using SPSS 25 software (IBM, Apache Software Foundation). The Kolmogorov–Smirnov test was used to check the normality of sample distribution. For comparisons between two experimental groups, a Student's *t* test was used in the case of normal sample distribution, whereas a nonparametric test (Mann–Whitney *U* test) was used in those cases in which normality could not be assumed. For multiple comparison, data were analyzed by a one-way ANOVA test. In those cases in which the one-way ANOVA was statistically significant, a Fisher LSD *post hoc* analysis was used to compare the differences between individual groups. Data from Sholl's analysis and regional AIS thickness were analyzed by a repeated-measures ANOVA test (Bolós et al., 2017). All statistical comparisons were performed on averaged values per animal. Graphs represent mean values ± SEM. A 95% CI was used for statistical comparisons. In Figures 2 and 3, asterisks indicate statistically significant differences with respect to 10-day-old newborn DGCs. In Figures 4, 5, and 6*E*, *F*, asterisks indicate statistically significant differences with respect to CH animals. In Figures 6*G–J* and 9*E*, *F*, asterisks indicate statistical significance in Tukey *post hoc* analyses. In Figures 7, 8, and 9*C*, *D*, *G*, asterisks indicate statistically significant differences with respect to PBS-treated animals.

Results

Morphological maturation of newborn DGCs

The experimental design is shown in a schematic diagram in Figure 1. Briefly, animals received a stereotaxic injection of a retrovirus that encodes the fluorescent protein Venus. After 10 d or 2, 3, 4, or 8 weeks, animals were sacrificed (Fig. 1*A*) and newborn DGCs were examined (Fig. 1*B*). The morphology (Fig. 1*C*), density of dendritic spines (Fig. 1*D*), AIS (Fig. 1*E*), and MFT area (Fig. 1*F*) were then analyzed.

Figure 2*A–E* shows representative images of the classical morphology of newborn DGCs at 10 d (Fig. 2*A*) and 2 (Fig. 2*B*), 3 (Fig. 2*C*), 4 (Fig. 2*D*), and 8 (Fig. 2*E*) weeks of age, together with high-power magnification images showing the presence of dendritic spines. As previously described (Zhao et al., 2006), the complexity of the dendritic trees increased with time. The total dendritic length (Fig. 2*F*) ($F_{(4,20)} = 216.642$; $p \leq 0.001$) and the number of dendritic branches, as measured by Sholl's analysis (repeated-measures ANOVA Greenhouse–Geisser interaction, $F = 46.762$; $p \leq 0.001$) (Fig. 2*G*), markedly increased as the cells matured. Moreover, we determined the density of dendritic spines as a measure of afferent connectivity. This parameter increased over time (Fig. 2*H*) ($F_{(4,20)} = 155.418$; $p \leq 0.001$). In addition, we questioned whether the MFTs of newborn DGCs exhibit morphological changes as the cells mature. Figure 2*I–M* shows representative images of the MFT morphology at 10 d (Fig. 2*I*), and 2 (Fig. 2*J*), 3 (Fig. 2*K*), 4 (Fig. 2*L*), and 8 (Fig. 2*M*) weeks of cell age. The area of individual MFTs (Fig. 2*N*) increased over time ($F_{(4,20)} = 30.349$; $p \leq 0.001$). Together, these data indicate that newborn DGCs undergo a profound morphological transformation over time, thereby also pointing to a parallel functional maturation of these cells, as previously demonstrated by other authors (van Praag et al., 2002; Zhao et al., 2006; Toni et al., 2008).

Dynamics of AIS development in newborn DGCs

Once we had ensured that our experimental design allowed the detection of morphological changes indicative of the functional transformation of newborn DGCs, we addressed whether the AIS also exhibited morphological changes during the maturation of these cells. Figure 3*A–C* shows representative *Z*-projection and high-power magnification images of the soma and the proximal domain of the axon of newborn DGCs at 10 d (Fig. 3*A*), and 3 weeks (Fig. 3*B*) and 8 weeks (Fig. 3*C*) of age. We first quantified the percentage of cells of each age with a clearly identifiable axon (Fig. 3*D*). This percentage increased over time ($F_{(4,20)} = 46.354$; $p \leq 0.001$). Next, we quantified the percentage of cells that showed a clearly identifiable AIS (Fig. 3*E*). To this end, orthogonal cross-sections were examined throughout the axon to confirm the colocalization between Venus and the AIS marker Ankyrin G. As an example, in Figure 3*A–C*, orthogonal YZ (right) and XZ (bottom) cross-sectional views of the axon obtained at axonal points located closer to the soma (Fig. 3*Aa*,*Ba*,*Ca*), and within (Fig. 3*Ab*,*Bb*,*Cb*) or beyond (Fig. 3*Ac*,*Bc*,*Cc*) the AIS location are shown. This percentage also increased over time ($F_{(4,20)} = 47.984$; $p \leq 0.001$). To study whether the establishment of axonal identity precedes AIS formation, we calculated the percentage of axons with a clearly identifiable AIS (Fig. 3*F*). As shown, not all the axonal projections had an AIS at earlier time points, although this percentage increased over time ($F_{(4,20)} = 6.477$; $p = 0.002$). These data support the notion that axon formation precedes that of AIS assembly. Accordingly, cells lacking a clearly identifiable axon did not show Ankyrin G expression in undifferentiated neurites.

Next, we performed an in-depth morphometric characterization of the AIS of newborn DGCs of different ages. AIS length increased with maturation ($F_{(4,20)} = 13.474$; $p \leq 0.001$) (Fig. 3*G*). In contrast, no changes in the AIS starting point were observed (Fig. 3*H*) ($F_{(4,20)} = 0.252$; $p = 0.315$). Moreover, we measured AIS thickness at different points of this structure, namely, proximal (the closest to the axonal hillock), medial, and distal (Fig. 3*I*). As shown, AIS thickness changed in the three locations as the DGCs matured (repeated-measures ANOVA Greenhouse–Geisser interaction, $F = 4.058$; $p = 0.025$), although a remarkable differential thickening of the proximal domain was evident in 4- and 8-week-old cells. Accordingly, the average AIS thickness increased at late maturational stages (Fig. 3*J*) ($F_{(4,20)} = 5.761$; $p = 0.003$).

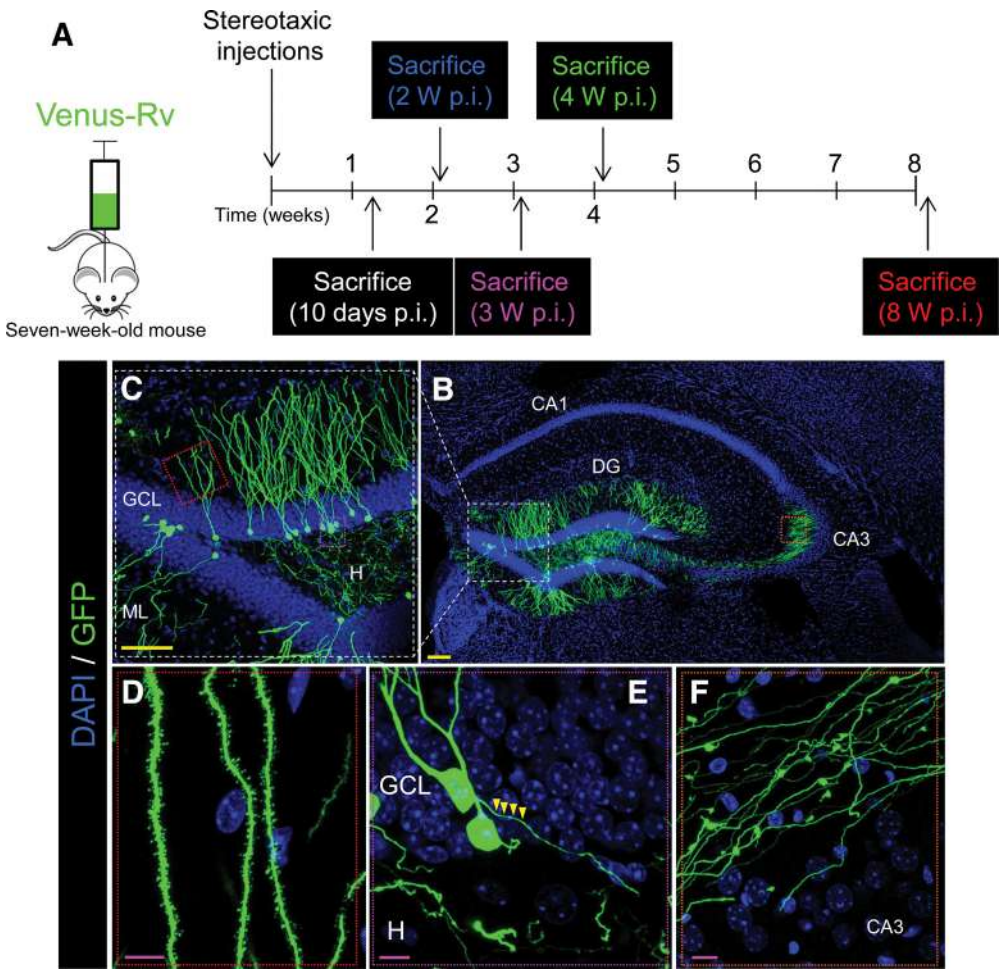

Figure 1. Experimental design. ***A***, Seven-week-old mice received a stereotaxic injection of a retrovirus that encodes the fluorescent protein Venus. After different periods of time (i.e., 10 d, and 2, 3, 4, or 8 weeks after injection), mice were sacrificed, and newborn DGCs were examined (***B***). ***C–F***, Representative images showing the morphology (***C***), dendritic spines (***D***), potential location of the AIS (***E***), and axonal terminals (named MFTs) (***F***) of 8-week-old newborn DGCs. Yellow scale bar, 100 μm. Pink scale bar, 10 μm. ***E***, Yellow triangles represent the potential location of the AIS.

EE accelerates the maturation of newborn DGCs

To test whether EE altered the morphological maturation of newborn DGCs during the initial period of AIS formation, mice were subjected to a 1 week period of EE or to CH conditions, starting 1 week after stereotaxic injections (Fig. 4*A*). Figure 4*B*, *C* provides representative images of the morphology of newborn DGCs, together with their respective high-power magnification images showing the presence of dendritic spines in CH (Fig. 4*B*) and EE (Fig. 4*C*) mice. EE accelerated the morphological maturation of the neurons, as reflected by the increase in total dendritic length (Fig. 4*D*) (Mann–Whitney $U = 1.000$; $p = 0.016$) and dendritic tree complexity, as shown by Sholl's analysis (Fig. 4*E*) (repeated-measures ANOVA Greenhouse–Geisser interaction, $F = 5.115$; $p = 0.013$).

We also analyzed the occurrence of indirect markers of somatic translocation phenomena (Murphy and Danzer, 2011) in newborn DGCs exposed to EE. In this regard, we found that EE increased the length of the primary apical dendrite (Mann–Whitney $U = 1.000$; $p = 0.016$) (Fig. 4*F*), whereas the percentage of cells with basal dendrites was not changed ($t = 1.978$; $p = 0.083$) (Fig. 4*G*). Moreover, EE did not alter migration into the GCL (Mann–Whitney $U = 12.000$; $p = 1.000$) (Fig. 4*H*) or the distance to the first change of axonal trajectory (Mann–Whitney $U = 11.000$; $p = 0.841$) (Fig. 4*I*). These data support the notion that EE accelerates the morphological maturation of newborn DGCs without triggering somatic translocation phenomena. Moreover, EE increased the density of dendritic spines (Fig. 4*J*) ($t = -2.273$; $p = 0.043$), although it did not change the area of individual MFTs (Fig. 4*K–M*) (Mann–Whitney $U = 11.000$; $p = 0.841$). Together, these data support previous evidence demonstrating that EE increases the morphological and functional maturation of DGCs (Alvarez et al., 2016).

EE alters the development of the AIS in newborn DGCs

Next, we addressed whether EE influenced the formation of the AIS in newborn DGCs. Figure 5*A*, *B*, shows representative images of this structure in animals subjected to either CH (Fig. 5*A*) or EE (Fig. 5*B*) conditions. Moreover, XZ and YZ orthogonal cross-sectional images obtained at different points of the axon located closer to the soma (Fig. 5*Aa*,*Ba*), and within (Fig. 5*Ab*,*Bb*), or beyond (Fig. 5*Ac*,*Bc*) the AIS location are shown to demonstrate that colocalization between Venus and Ankyrin G occurred only within the AIS region.

EE increased the percentage of cells with a clearly identifiable axon (Fig. 5*C*) (Mann–Whitney $U = 2.000$; $p = 0.028$) and tended to increase the percentage of cells with an AIS (Fig. 5*D*) (Mann–Whitney $U = 3.000$; $p = 0.056$). However, it did not

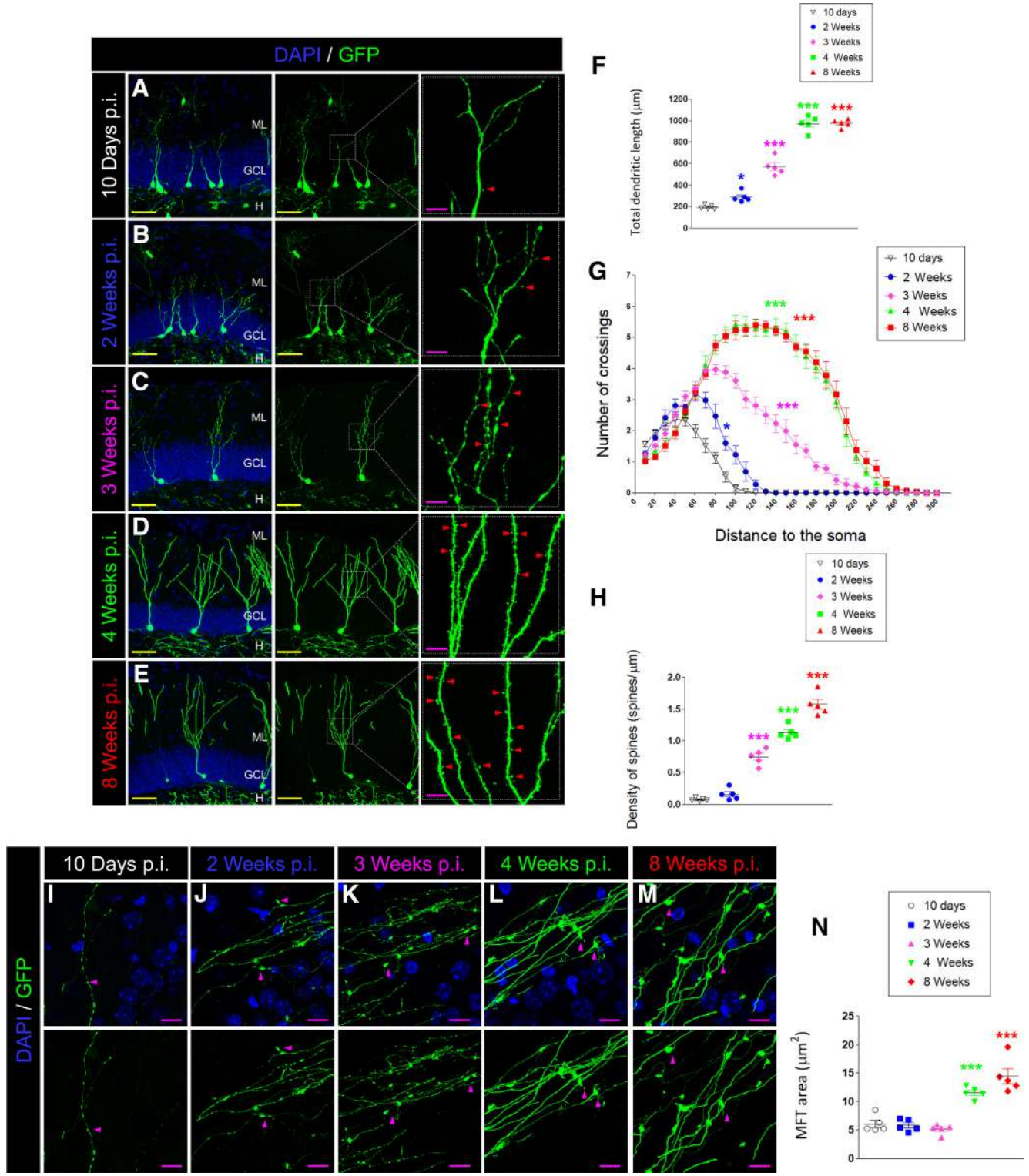

Figure 2. Maturation of newborn DGCs. ***A–E***, Representative images of 10-day-old (***A***) and 2- (***B***), 3- (***C***), 4- (***D***), or 8- (***E***) week-old newborn DGCs and their respective high-power magnification images showing the presence of dendritic spines (red triangles). ***F***, Total dendritic length in cells of different ages. ***G***, Sholl's analysis of dendritic branching. ***H***, Density of dendritic spines. ***I–M***, Representative high-power magnification images of MFTs of 10-day-old (***I***) and 2- (***J***), 3- (***K***), 4- (***L***), or 8- (***M***) week-old newborn DGCs. ***N***, Area of individual MFTs. Yellow scale bar, 50 μm. Pink scale bar, 10 μm. Red triangles represent dendritic spines. Pink triangles represent MFTs. *$0.05 > p \geq 0.01$. ***$0.001 \geq p$. Asterisks indicate statistically significant differences with respect to 10-day-old newborn DGCs. Error bars represent SEM.

change the percentage of axons exhibiting an AIS (Fig. 5*E*) ($t = -1.224$; $p = 0.256$). In contrast, EE increased the length (Fig. 5*F*) (Mann–Whitney $U = 2.500$; $p = 0.047$) and distance between the axonal hillock and the AIS starting point (Fig. 5*G*) ($t = -2.422$; $p = 0.042$). However, EE did not alter the thickness of this structure (Fig. 5*H*) ($t = 0.391$; $p = 0.707$). These data demonstrate that EE induces the remodeling of the morphological properties and position of the AIS of newborn DGCs.

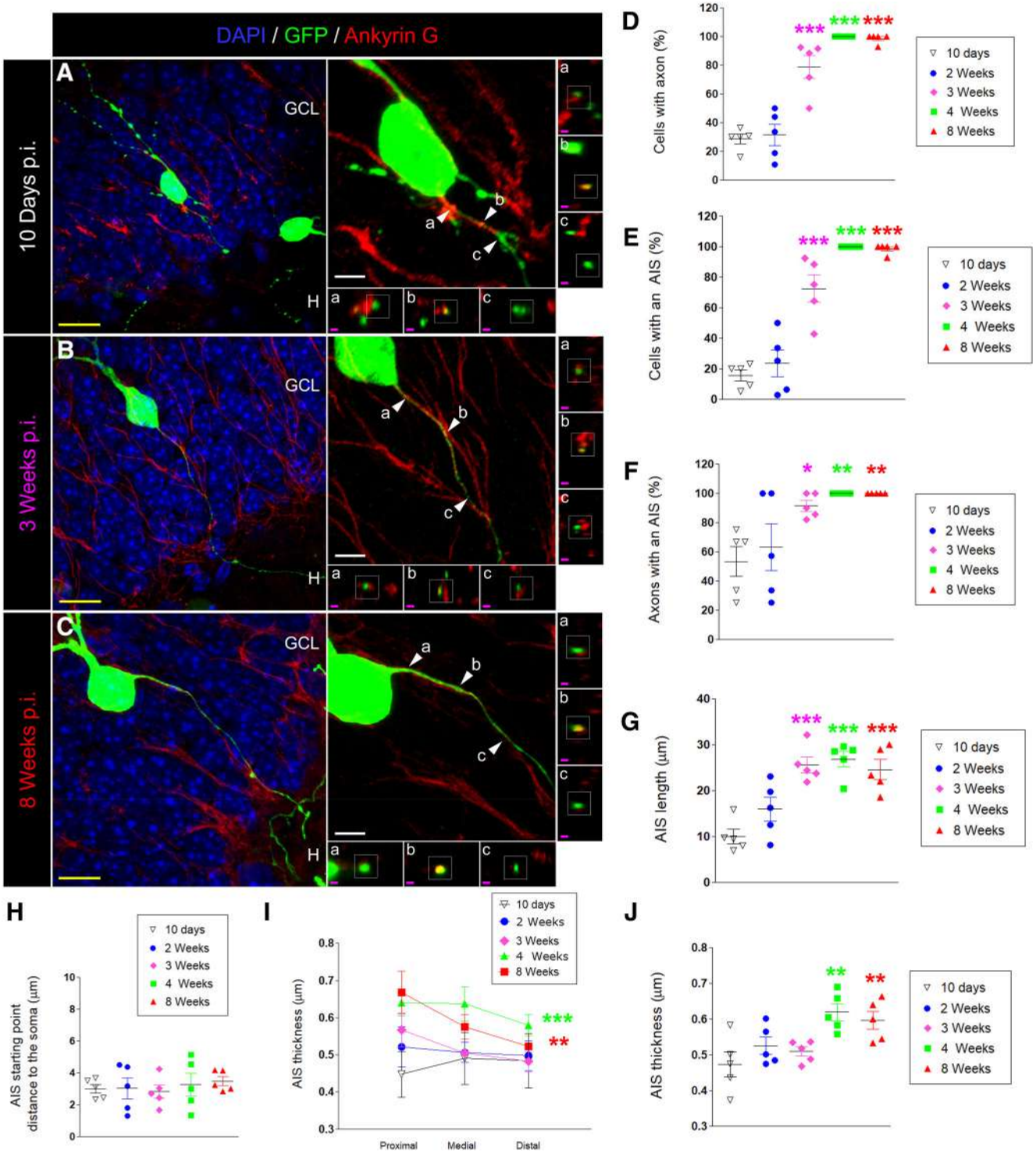

Figure 3. AIS formation during adult hippocampal neurogenesis. ***A–C***, Representative images of the AIS of 10-day-old (***A***) and 3- (***B***) or 8- (***C***) week-old newborn DGCs. To visualize the starting and ending point of the AIS, orthogonal cross-sections were examined throughout the axon to detect the colocalization between Venus and the AIS marker Ankyrin G. As an example, orthogonal YZ (right) and XZ (bottom) cross-sectional views of the axon obtained at axonal points located closer to the soma (***a***), within (***b***), and beyond (***c***) the AIS location are shown. ***D***, Percentage of cells with a clearly identifiable axonal projection. ***E***, Percentage of cells with a clearly identifiable AIS. ***F***, Percentage of axons with a clearly identifiable AIS. ***G***, AIS length. ***H***, AIS starting point. ***I***, Thickness at the proximal, medial, and distal points of the AIS. ***J***, Average AIS thickness. Yellow scale bar, 10 μm. White scale bar, 5 μm. Pink scale bar, 1 μm. *$0.05 > p \geq 0.01$. **$0.01 > p \geq 0.001$. ***$0.001 \geq p$. Asterisks indicate statistically significant differences with respect to 10-day-old newborn DGCs. Error bars represent SEM.

EE increases the activation of newborn DGCs

To further characterize the mechanisms through which EE accelerated the maturation of newborn DGCs, we next studied the expression of cfos, an early immediate gene that shows nuclear localization under conditions of neuronal activation (Morgan and Curran, 1989), in the GCL of CH and EE animals (Fig. 6*A–D*). EE did not modify the global density of cfos$^+$ nuclei in this layer (Fig. 6*E*) ($t = 0.646$; $p = 0.576$). Instead, it markedly increased the proportion of newborn Venus$^+$ cells that showed nuclear expression of cfos (Fig. 4*F*) ($t = 5.042$; $p = 0.001$). These

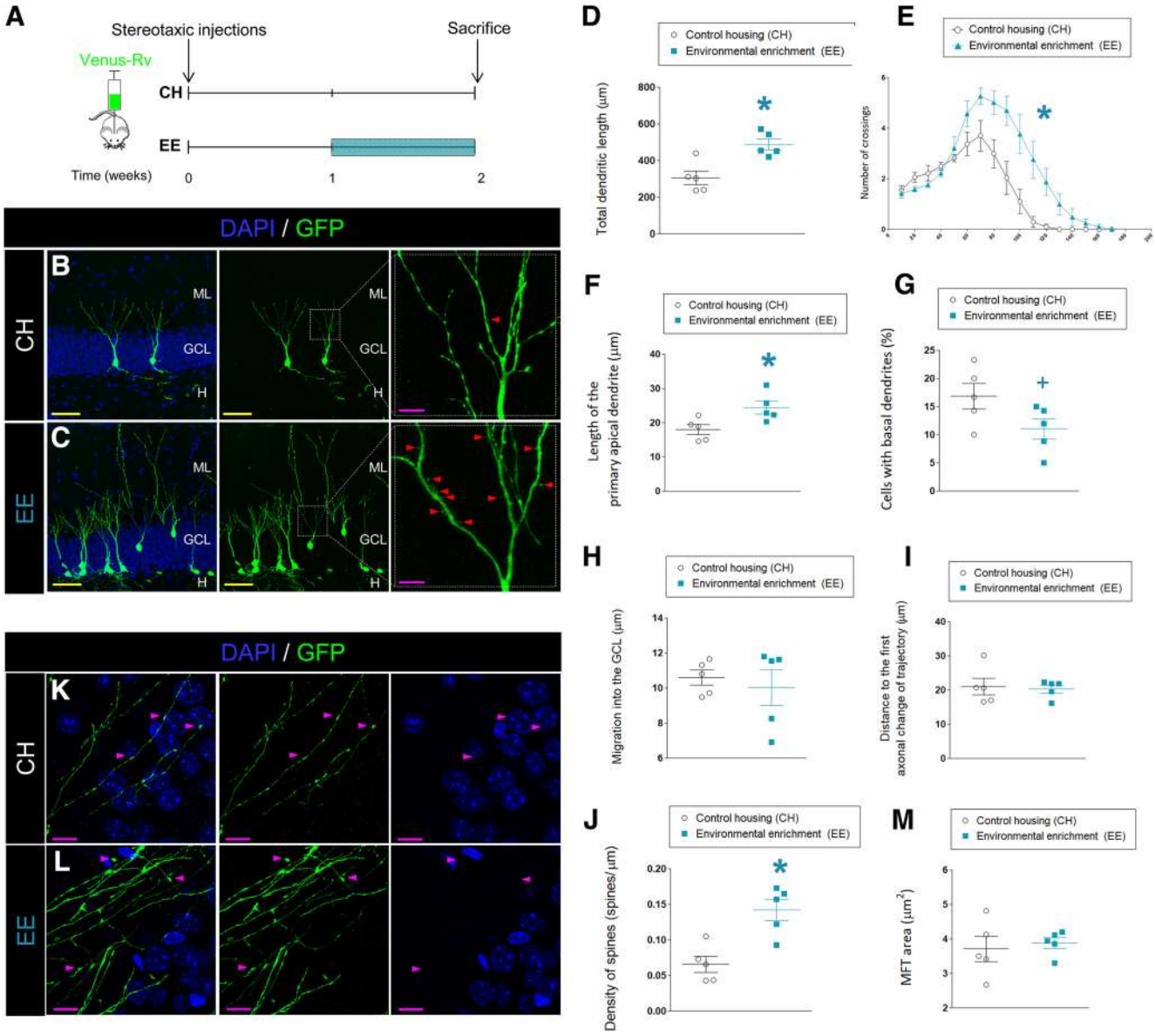

Figure 4. EE accelerates the maturation of newborn DGCs. ***A***, Schematic experimental design. Briefly, animals received a stereotaxic injection of a retrovirus that encodes the fluorescent protein Venus. One week later, half the animals were exposed to a week of EE, whereas the other half were housed under standard conditions. ***B***, ***C***, Representative images of newborn DGCs belonging to CH (***A***) or EE (***B***) mice, together with their respective high-power magnification images showing the presence of dendritic spines. ***D***, Total dendritic length. ***E***, Sholl's analysis of dendritic branching. ***F***, Length of the primary apical dendrite. ***G***, Percentage of cells with basal dendrites. ***H***, Migration into the GCL. ***I***, Distance between the axonal hillock and the first change of axonal trajectory. ***J***, Density of dendritic spines. ***K***, ***L***, Representative high-power magnification images of MFTs of newborn DGCs belonging to CH (***K***) and EE (***L***) animals. ***M***, Area of individual MFTs. Yellow scale bar, 50 μm. Pink scale bar, 10 μm. Red triangles represent dendritic spines. Pink triangles represent MFTs. *$0.05 > p \geq 0.01$. Error bars represent SEM.

data indicate that EE selectively increases the activation of newborn DGCs.

Next, we questioned whether the changes in neuronal activation correlated with morphological differences in the AIS of these cells. To this end, we measured various morphometric parameters in the AIS of cfos$^+$ and cfos$^-$ cells of CH and EE animals (Fig. 6*G–J*). The percentage of cells that showed a clearly identifiable axonal projection (Fig. 6*G*) (one-way ANOVA, $F_{(4,20)} = 20.96$; $p \leq 0.001$; Tukey *post hoc* analyses: CH, $p \leq 0.001$; EE, $p = 0.002$) and an AIS (Fig. 6*H*) (one-way ANOVA, $F_{(4,20)} = 14.06$; $p \leq 0.001$; Tukey *post hoc* analyses: CH, $p \leq 0.001$; EE, $p = 0.003$) was remarkably higher in cfos$^+$ cells. Moreover, marked differences in AIS morphometric parameters between cfos$^+$ and cfos$^-$ cells were observed. In this regard, the AIS of cfos$^+$ cells appeared to be farther from the soma (Fig. 6*I*) (one-way ANOVA, $F_{(4,20)} = 16.60$; $p \leq 0.001$; Tukey *post hoc* analyses: CH, $p = 0.003$; EE, $p \leq 0.001$) and was longer (Fig. 6*J*) (one-way ANOVA, $F_{(4,20)} = 18.16$; $p \leq 0.001$; Tukey *post hoc* analyses: CH, $p = 0.002$; EE, $p \leq 0.001$) than that of cfos$^-$ cells. These data indicate that neuronal activation correlates with changes in the morphological properties of the AIS during newborn DGC maturation.

LPS impairs the maturation of newborn DGCs

To study the effects of LPS on the maturation of newborn DGCs, mice were implanted with subcutaneous osmotic pumps filled with either LPS or PBS, which were administered continuously for 2 weeks (Fig. 7*A–C*). LPS did not cause remarkable effects on the morphology of the neurons (Fig. 7*D*,*E*), nor did it alter total dendritic length (Fig. 7*D*) ($t = 0.345$; $p = 0.744$) or dendritic branching, as measured by Sholl's analysis (Fig. 7*E*) (repeated-

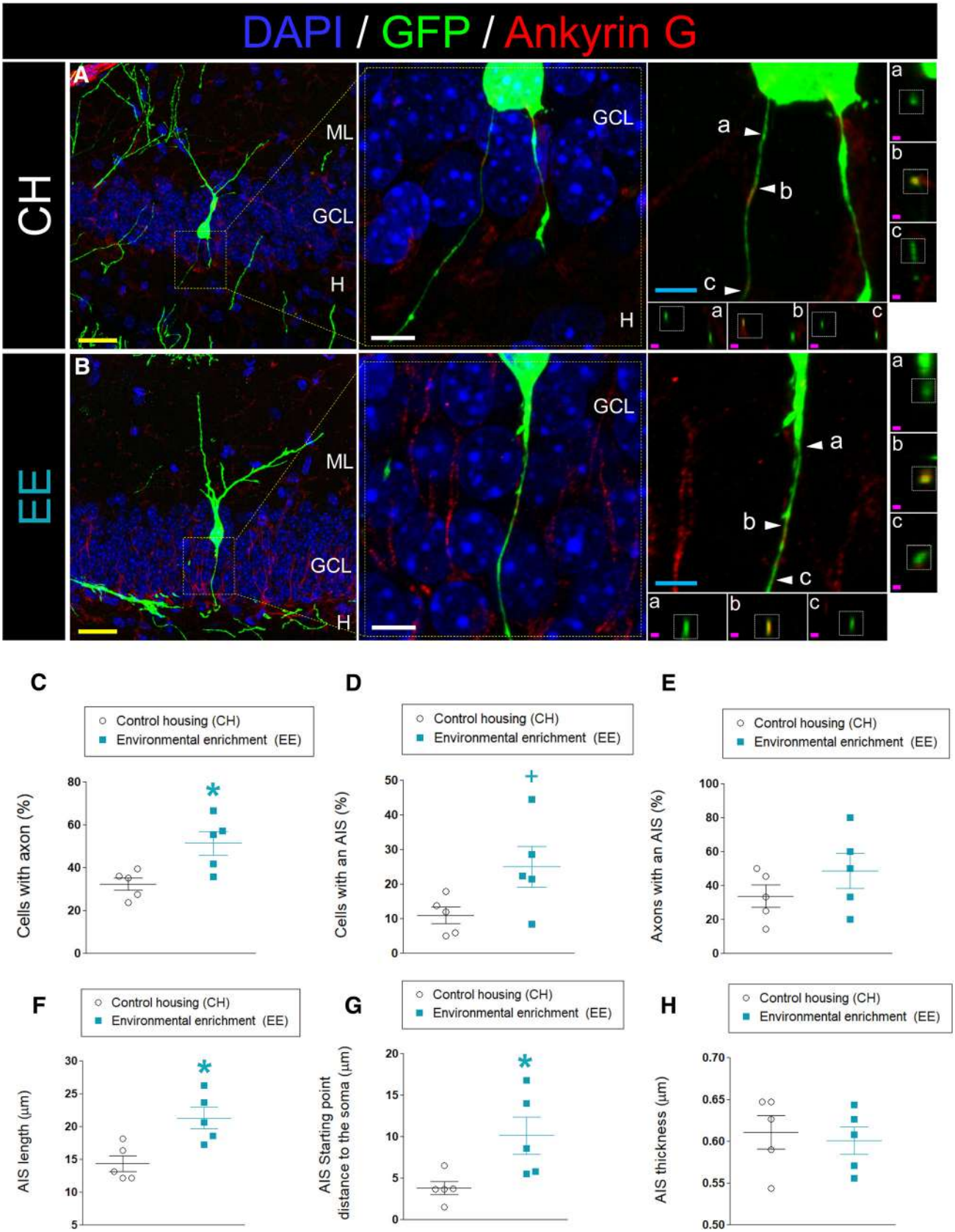

Figure 5. EE effects on the development of the AIS of newborn DGCs. ***A***, ***B***, Representative images of newborn DGCs belonging to animals exposed to CH (***A***) and EE (***B***). To visualize the starting and ending point of the AIS, XZ and YZ orthogonal cross-sectional images obtained at different points of the axon located closer to the soma (***a***), and within (***b***) or beyond (***c***) the AIS location are shown. It should be noted that colocalization between Venus and Ankyrin G occurred only within the AIS region. ***C***, Percentage of cells with a clearly identifiable axonal projection. ***D***, Percentage of cells with a clearly identifiable AIS. ***E***, Percentage of axons with a clearly identifiable AIS. ***F***, AIS length. ***G***, AIS starting point. ***H***, Average AIS thickness. Yellow scale bar, 50 μm. White scale bar, 10 μm. Blue scale bar, 5 μm. Pink scale bar, 1 μm. *$0.05 > p \geq 0.01$. $^{+}$ $0.1 > p \geq 0.05$. Error bars represent SEM.

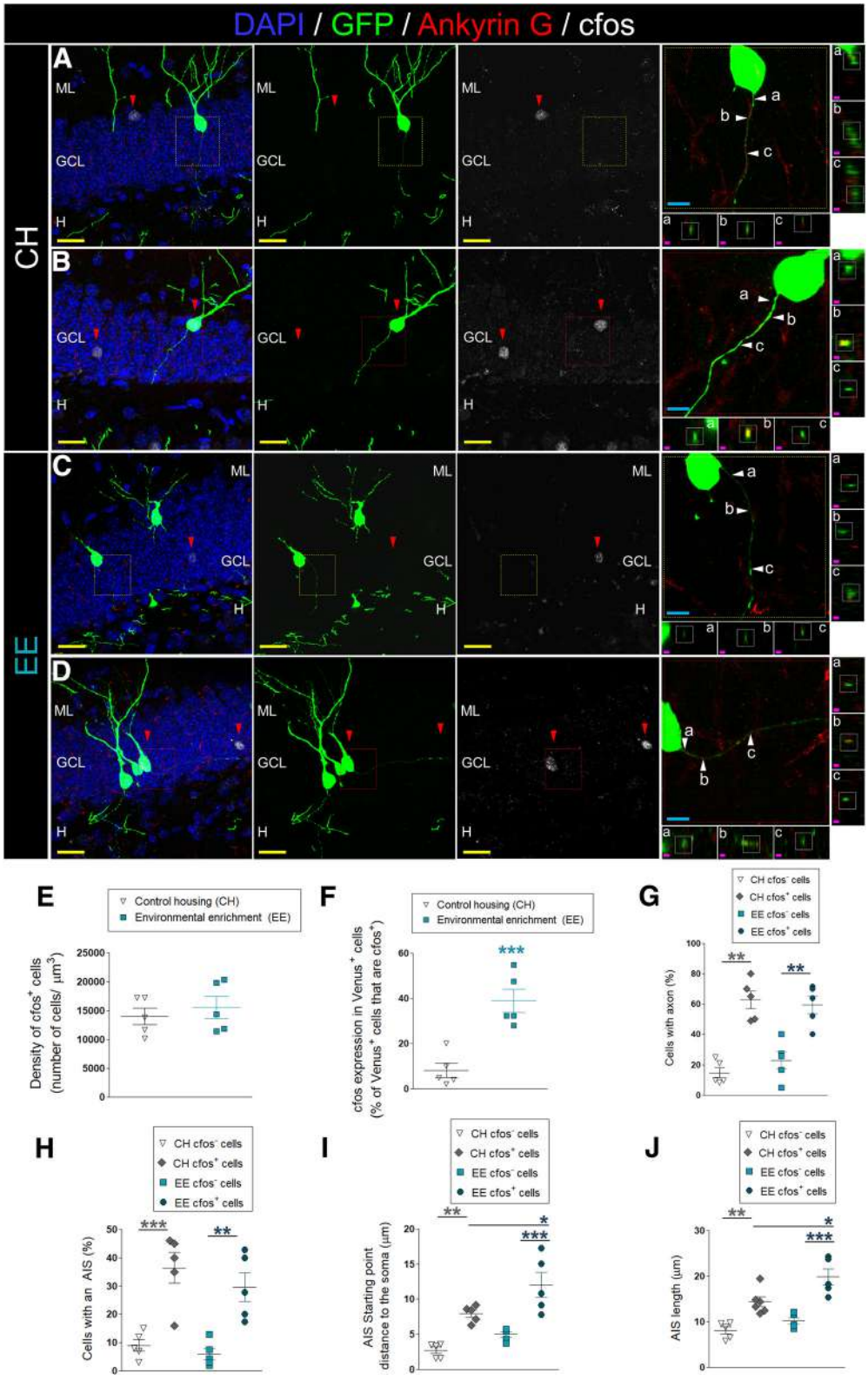

Figure 6. EE effects on the activation of newborn DGCs. ***A–D***, Representative images of cfos $^{-}$ (***A***,***C***) and cfos $^{+}$ (***B***,***D***) cells in CH (***A***,***B***) and EE (***C***,***D***) animals. To visualize the starting and ending point of the AIS, XZ and YZ orthogonal cross-sectional images obtained at different points of the axon located closer to the soma (***Aa***,***Ba***,***Ca***,***Da***), and within (***Ab***,***Bb***,***Cb***,***Db***) or beyond (***Ac***,***Bc***,***Cc***,***Dc***) the AIS location are shown. ***E***, Density of cfos $^{+}$ nuclei in the GCL. ***F***, Percentage of Venus $^{+}$ cells that show cfos nuclear staining. ***G***, Percentage of cfos $^{+}$/Venus $^{+}$ and cfos $^{-}$/Venus $^{+}$ cells with a clearly identifiable axonal projection. ***H***, Percentage of cfos $^{+}$/Venus $^{+}$ and cfos $^{-}$/Venus $^{+}$ cells with a clearly identifiable AIS. ***I***, AIS starting point in cfos $^{+}$/Venus $^{+}$ and cfos $^{-}$/Venus $^{+}$ cells. ***J***, AIS length in cfos $^{+}$/Venus $^{+}$ and cfos $^{-}$/Venus $^{+}$ cells. Yellow squares represent Venus $^{+}$/cfos $^{-}$ cells. Red squares represent Venus $^{+}$/cfos $^{+}$ cells. Red triangles represent cfos $^{+}$ cells. Yellow scale bar, 50 μm. Blue scale bar, 5 μm. Pink scale bar, 1 μm. ***E***, ***F***, Asterisks indicate differences with CH animals. ***G***, ***J***, Asterisks indicate statistical significance in Tukey *post hoc* analyses. *$0.05 > p \geq 0.01$. **$0.01 > p \geq 0.001$. ***$0.001 \geq p$. Error bars represent SEM.

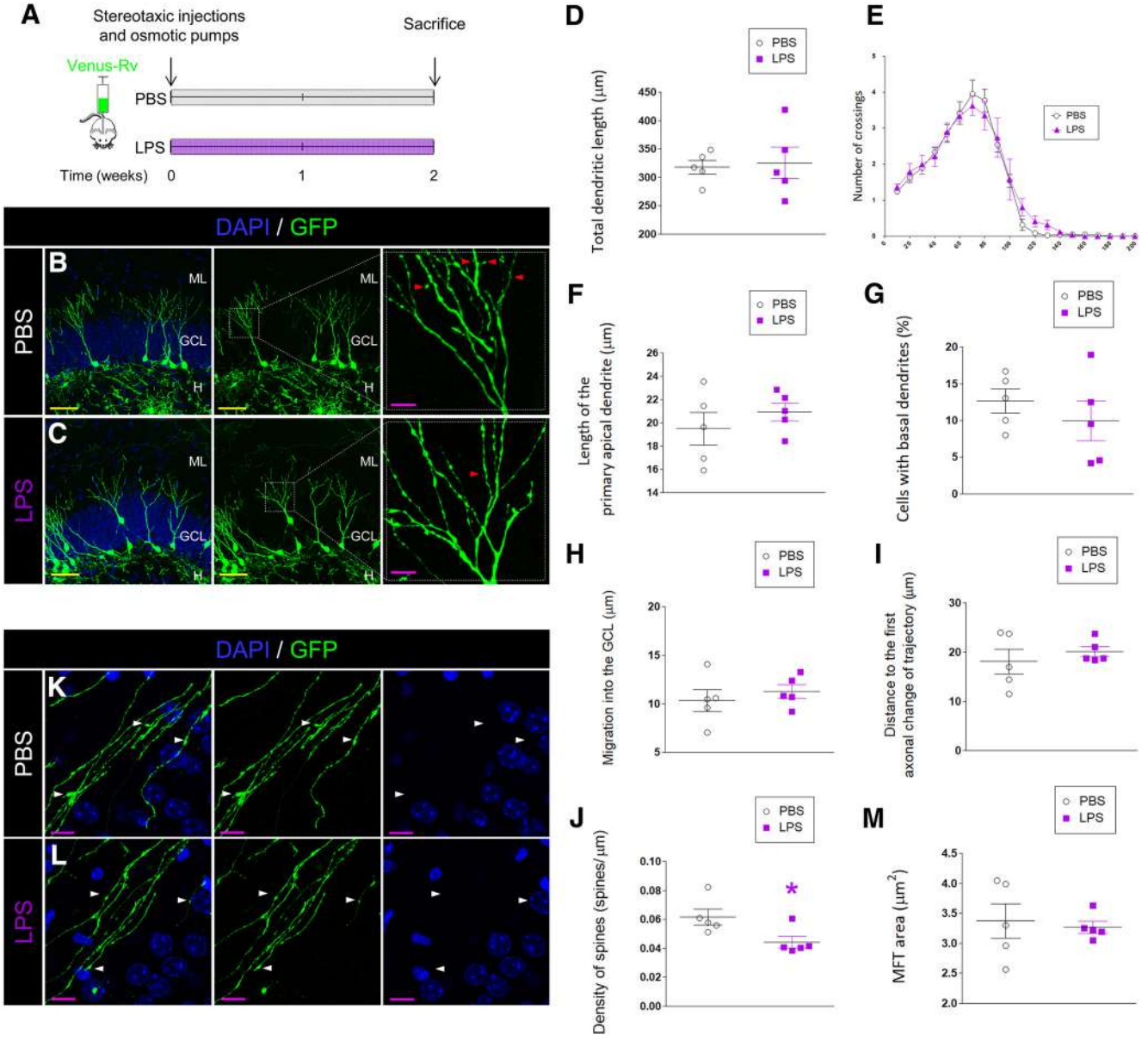

Figure 7. LPS from *E. coli* impairs the maturation of newborn DGCs. ***A***, Schematic experimental design. Briefly, animals received a stereotaxic injection of a retrovirus that encodes the fluorescent protein Venus and were implanted with osmotic pumps filled with PBS or LPS. Two weeks later, animals were sacrificed. ***B***, ***C***, Representative images of newborn DGCs belonging to PBS-treated (***B***) or LPS-treated (***C***) animals, together with their respective high-power magnification images showing the presence of dendritic spines. ***D***, Total dendritic length. ***E***, Sholl's analysis of dendritic branching. ***F***, Length of the primary apical dendrite. ***G***, Percentage of cells with basal dendrites. ***H***, Migration into the GCL. ***I***, Distance between the axonal hillock and the first change of axonal trajectory. ***J***, Density of dendritic spines. ***K***, ***L***, Representative high-power magnification images of MFTs of newborn DGCs belonging to PBS-treated (***K***) or LPS-treated (***L***) animals. ***M***, Quantification of the area of individual MFTs. Yellow scale bar, 50 μm. Pink scale bar, 10 μm. Red triangles represent dendritic spines. White triangles represent MFTs. *$0.05 > p \geq 0.01$. Error bars represent SEM.

measures ANOVA, Greenhouse–Geisser interaction, $F = 0.683$; $p = 0.672$). Neither did LPS change the length of the primary apical dendrite (Fig. 7*F*) ($t = -0.895$; $p = 0.404$), the percentage of cells with basal dendrites (Fig. 7*G*) ($t = 0.845$; $p = 0.428$), the migration of these cells into the GCL (Fig. 7*H*) ($t = -0.69$; $p = 0.513$), or the distance between the axonal hillock and the first change of axonal trajectory (Fig. 7*I*) ($t = -0.743$; $p = 0.489$). However, LPS reduced the density of dendritic spines (Fig. 7*J*) ($t = 2.326$; $p = 0.048$) but had no effect on the area of the MFTs of newborn DGCs (Fig. 7*K–M*) ($t = 0.345$; $p = 0.744$). Together, these data indicate that LPS alters the structural plasticity of newborn DGCs, as we and others have previously demonstrated (Ekdahl et al., 2003; Monje et al., 2003; Llorens-Martín et al., 2014).

LPS alters the development of the AIS in newborn DGCs

Next, we addressed whether LPS administration modified AIS formation in newborn DGCs. Figure 8*A*, *B*, shows representative images of this structure in animals that received PBS (Fig. 8*A*) or LPS (Fig. 8*B*). Moreover, XZ and YZ orthogonal cross-sectional images obtained at different points of the axon located closer to the soma (Fig. 8*Aa*,*Ba*), and within (Fig. 8*Ab*,*Bb*) or beyond (Fig. 8*Ac*,*Bc*) the AIS location are shown to demonstrate that colocalization between Venus and Ankyrin G occurred only within the AIS region.

LPS increased the percentage of cells with a clearly identifiable axon (Fig. 8*C*) (Mann–Whitney $U = 0.000$; $p = 0.008$) and caused a nonsignificant trend to reduce the percentage of cells

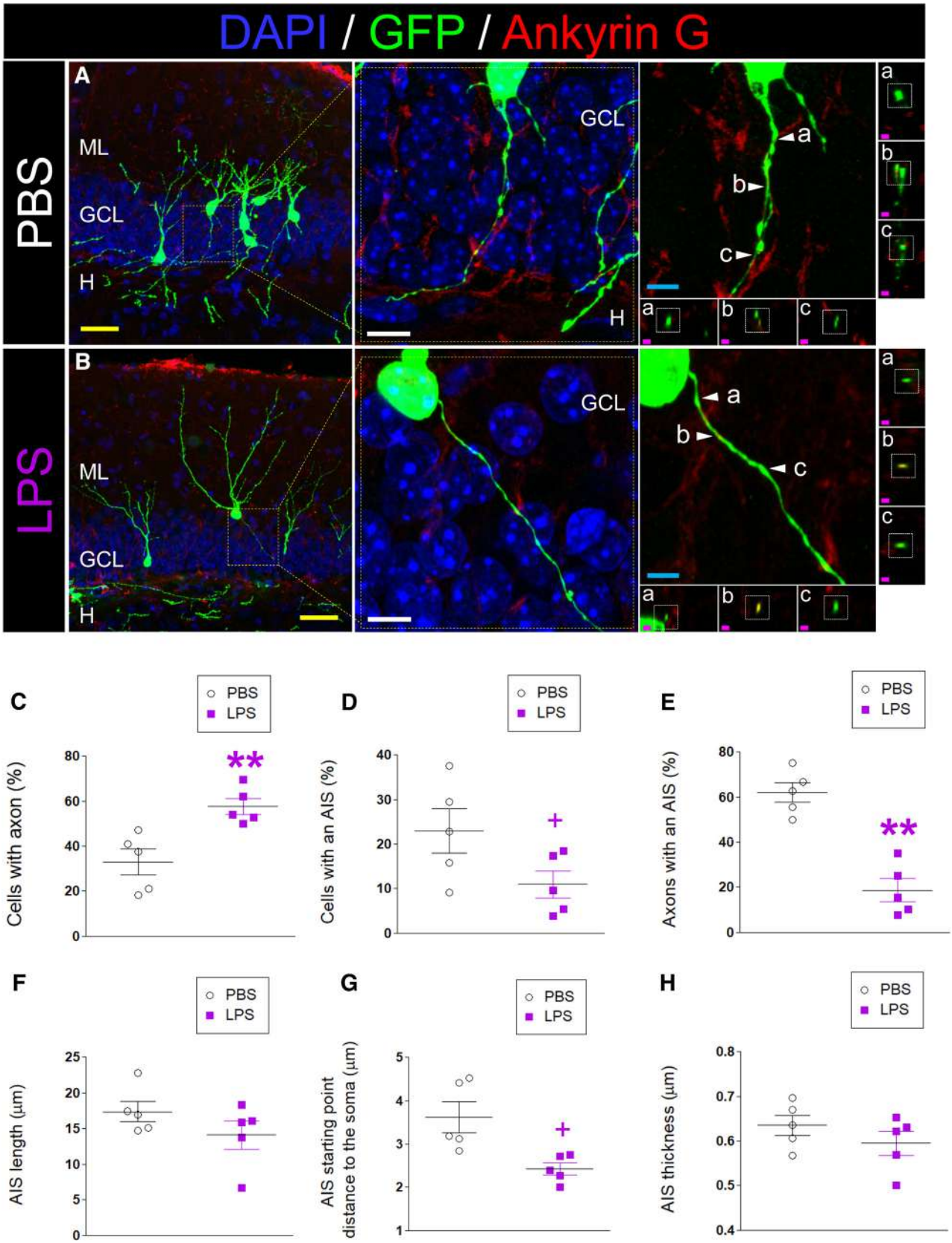

Figure 8. LPS from *E. coli* alters the development of the AIS of newborn DGCs. ***A***, ***B***, Representative images of newborn DGCs belonging to PBS-treated (***A***) or LPS-treated (EE) (***B***) mice. To visualize the starting and ending point of the AIS, XZ, and YZ orthogonal cross-sectional images obtained at different points of the axon closer to the soma (***a***), and within (***b***) or beyond (***c***) the AIS location are shown. It should be noted that colocalization between Venus and Ankyrin G occurred only within the AIS region. ***C***, Percentage of cells with a clearly identifiable axonal projection. ***D***, Percentage of cells with a clearly identifiable AIS. ***E***, Percentage of axons with a clearly identifiable AIS. ***F***, AIS length. ***G***, AIS starting point. ***H***, Average AIS thickness. Yellow scale bar, 50 μm. White scale bar, 10 μm. Blue scale bar, 5 μm. Pink scale bar, 1 μm. $^{+}0.1 > p \geq 0.05$. $^{**}0.01 > p \geq 0.001$. Asterisks indicate statistically significant differences with respect to PBS-treated mice. Error bars represent SEM.

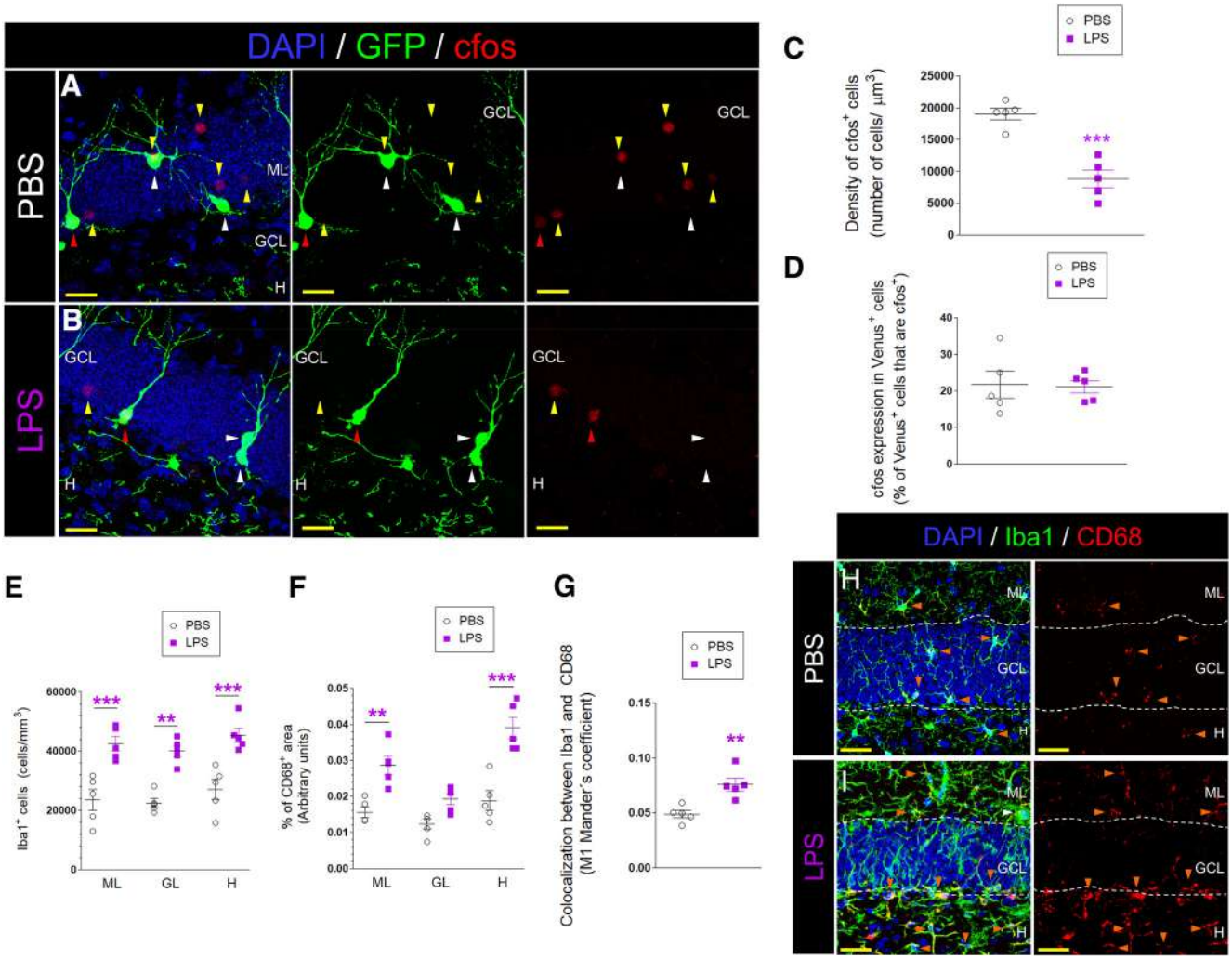

Figure 9. Effects of LPS from *E. coli* on newborn DGC activation and neuroinflammation in the DG. ***A***, ***B***, Representative images of the DG belonging to PBS-treated (***A***) or LPS-treated (EE) (***B***) mice, showing cfos staining (red) and retrovirally labeled newborn DGCs (green). ***C***, Density of cfos $^{+}$ nuclei in the GCL. ***D***, Percentage of Venus $^{+}$ cells that show cfos nuclear staining. ***E–I***, Microglial activation in the DG. ***E***, Density of Iba1 $^{+}$ microglial dells in the ML, GCL, and H. ***F***, Intensity of CD68 fluorescence signal in the ML, GCL, and H. ***G***, M1 Mander's coefficient showing colocalization between Iba1 and CD68. ***H***, ***I***, Representative images showing staining with Iba1 and CD68 in the DG of PBS-treated (***H***) or LPS-treated (***I***) animals. Yellow scale bar, 50 μm. Yellow triangles represent Venus $^{-}$/cfos $^{+}$ cells. Red triangles represent Venus $^{+}$/cfos $^{+}$ cells. White triangles represent Venus $^{+}$/cfos $^{-}$ cells. Orange triangles represent microglial cells. **$0.01 > p \geq 0.001$. ***$0.001 \geq p$. Error bars represent SEM.

that had an AIS (Fig. 8*D*) ($t = 2.028$; $p = 0.077$). As a result, LPS reduced the percentage of axons exhibiting a clearly identifiable AIS (Fig. 8*E*) (Mann–Whitney $U = 0.000$; $p = 0.008$). Moreover, this treatment did not lead to a change in AIS length (Fig. 8*F*) (Mann–Whitney $U = 11.000$; $p = 0.841$), distance between the soma and the AIS starting point (Fig. 8*G*) (Mann–Whitney $U = 3.000$; $p = 0.056$), or AIS thickness (Fig. 8*H*) ($t = 1.140$; $p = 0.288$).

Effects of LPS on the activation of DGCs and microglia in the DG

Next, we addressed whether exposure to LPS altered the activation of the population of granule neurons (Fig. 9*A–D*). To this end, we quantified the number of cfos $^{+}$ cells in the GCL of PBS- and LPS-treated animals. We found a marked reduction in the density of cfos $^{+}$ cells in the latter (Fig. 9*C*) ($t = 6.319$; $p \leq 0.001$). However, this reduction was not observed among Venus $^{+}$ cells (Fig. 9*D*) ($t = 0.132$; $p = 0.898$).

Given that no changes in newborn DGC activation were observed in LPS-treated animals, we studied whether a shift toward a proinflammatory milieu in the DG caused by LPS administration correlated with the differences in the AIS development observed in these animals (Fig. 9*E–I*). To this end, we quantified the number of Iba1 $^{+}$ microglial cells located in the ML, GCL, and H. Supporting previous observations (Llorens-Martín et al., 2014), we found that LPS treatment increased the number of microglial cells in the three regions (Fig. 9*E*) (one-way ANOVA, $F_{(5,29)} = 14.95$; $p \leq 0.001$; Tukey *post hoc* analyses: ML, $p \leq 0.001$; GCL, $p = 0.01$; H, $p \leq 0.001$). Moreover, to further characterize the activation status of microglial cells in the aforementioned regions of the DG, we studied the expression of the microglial activation marker CD68 (Llorens-Martín et al., 2016) in these cells (Fig. 9*F–I*). LPS increased the expression of CD68, and this increase was specific to the ML and H (one-way ANOVA, $F_{(5,29)} = 20.19$; $p \leq 0.001$; Tukey *post hoc* analyses: ML, $p = 0.01$; GCL, $p = 0.242$; H, $p \leq 0.001$) (Fig. 9*F*). Moreover, the percentage of Iba1 $^{+}$ area that was CD68 $^{+}$ (M1 Mander's colocalization coefficient) was accordingly increased ($t = 4.067$; $p = 0.0036$) (Fig. 9*G*). In Figure 9*H*, *I*, representative images show the differences in microglial cell numbers and CD68 expression previously described. To-

gether, these data demonstrate that the administration of LPS triggers a shift toward a proinflammatory milieu in the DG and that this effect occurs in parallel to the alteration in the development of the AIS of newborn DGCs.

Discussion

AHN encompasses various stages and leads to the integration of newborn DGCs into the trisynaptic circuit (Zhao et al., 2006). Early after immature neuroblasts are committed to the neuronal lineage, their morphology is characterized by the presence of several undifferentiated neurites. At 10–11 d of cell age, axonal fibers are observed in the CA3 and CA2 hippocampal subfields (Zhao et al., 2006; Llorens-Martín et al., 2015b). Given that only 30% of 10-day-old newborn DGCs showed a clearly identifiable axonal projection, while most of the cells showed only undifferentiated neurites, our data support the notion that there are marked maturational differences between individual cells at early time points. Nevertheless, this heterogeneity seems to disappear at the fourth week of cell age because ~100% of the cells showed a clearly identifiable axon at this age. Accordingly, this generalized axonal identity establishment is accompanied by a series of cellular events that are indicative of subsequent functional maturation of the cells, such as the marked increase in dendritic length and branching and in the density of dendritic spines.

We have analyzed the temporal dynamics of AIS formation in newborn DGCs of young adult mice *in vivo*. In this regard, the AIS was absent in cells with undifferentiated neurites and that lacked a clearly identifiable axon. Moreover, at 10 d of cell age, only 50% of the axons had an AIS, whereas this percentage increased as the postinjection interval extended, reaching a plateau at 3 or 4 weeks of cell age. In this regard, our data support previous *in vitro* (Rasband, 2010) and *in vivo* (Galiano et al., 2012) evidence showing that axonal determination precedes AIS formation and that the latter process is regulated by intrinsic maturational programs (Petersen et al., 2017).

Interestingly, the period in which the AIS of newborn DGCs exhibited the greatest structural changes (i.e., the period comprised between the second and the third weeks of cell age) coincided with the period of highest dendritic remodeling. Notably, AIS formation preceded the marked increase in the area of MFTs, which occurred at 4 weeks of age. Given the high density of Na(v) channels present in the AIS (50 times compared with the somatodendritic compartment) (Kole et al., 2008), this structure is the most favorable site for AP initiation (Colbert and Johnston, 1996; Kole et al., 2008; Kole and Stuart, 2012). Thus, it can be hypothesized that the presence of a functional AIS is required for the establishment of mature synaptic contacts with efferent targets. Indeed, certain aspects of the AIS structure that might be related to the efficiency of AP generation, such as the differences in thickness between the proximal and the distal zones of the AIS (Petersen et al., 2017; González-Cabrera et al., 2017), were observable only in 4- and 8-week-old newborn DGCs, whereas no marked regional differences in AIS thickness were detected in younger cells.

In this regard, the structural features of the AIS have an enormous impact on the functionality of developing neurons (Evans et al., 2015; Yamada and Kuba, 2016). For instance, both AIS length and distance from the axonal hillock correlate with the excitability of these cells (Kuba, 2012; Evans et al., 2015; Yamada and Kuba, 2016). In general terms, longer AISs located closer to the axon hillock are more efficient in generating APs because the number of ion channels present in the structure are directly proportional to the AIS surface (length), and short distances between the axonal hillock and the AIS starting point reduce the dissipation of charges during propagation from the soma (Yamada and Kuba, 2016). However, an elegant study by Gulledge and Bravo (2016) has recently brought to light another crucial level of complexity in the dependence between AIS structure and function and have introduced the concept of the "optimal" AIS conformation. This conformation is defined as the AIS length and position that render minimal rheobase currents and the highest probability of AP generation (Gulledge and Bravo, 2016). Those authors showed that dendritic morphology determines the "optimal" AIS conformation. This novel and revolutionary concept has reshaped our current knowledge about the AIS and has been further supported by the work of other authors (Hamada et al., 2016). Gulledge and Bravo (2016) proposed a shorter AIS as an "optimal" conformation for neurons with low dendritic capacitance and a longer AIS as "optimal" for neurons with higher dendritic capacitance. According to this model, AIS lengthening is the most efficient mechanism through which to counteract the reduced excitability caused by increased dendritic capacitance (Gulledge and Bravo, 2016). Thus, our data suggest that AIS lengthening in mature neurons might be an "optimal" AIS conformation that allows the adjustment of cellular excitability to higher dendritic capacitance.

In this regard, several examples of AIS structural remodeling during neuronal development are found in the literature (Conradi and Ronnevi, 1977; Gutzmann et al., 2014; Kuba et al., 2014; Nozari et al., 2017; Schlüter et al., 2017). Moreover, previous evidence shows that the structural development of the AIS can be extrinsically modulated during neuronal maturation. For instance, elegant work by Kuba et al. (2010) demonstrated that auditory stimuli deprivation results in the lengthening of the AIS of avian brainstem auditory neurons. Similar results were obtained by Schlüter et al. (2017) when testing visual deprivation. Other studies by Evans et al. (2015) showed that cultured hippocampal neurons subjected to continuous depolarization responded with rapid AIS shortening or distancing (Grubb and Burrone, 2010). Moreover, previous data support the notion that external stimuli, such as EE, modulate the structural plasticity of the AIS of cortical neurons during a restricted developmental period (Nozari et al., 2017). In agreement with that study, our findings reveal that extrinsic factors can modulate the dynamics of AIS formation in newborn DGCs of young adult mice *in vivo*. In this regard, EE is one of the most potent positive modulators of AHN (Kempermann et al., 1997), although newborn DGCs exhibit variable sensitivity to the effects of EE throughout their maturation (Bergami et al., 2015; Alvarez et al., 2016). Indeed, our data show that a 1 week period of EE does not induce a general activation of the population of DGCs but rather a selective increase in the percentage of Venus$^+$ newborn DGCs that show nuclear expression of cfos. Given the specific increase in the activation of this population of cells, we explored the consequences of this manipulation on the formation of their AIS. EE was observed to trigger the distancing of the AIS from the soma and the lengthening of this structure. Importantly, these effects were more evident in cfos$^+$ cells, thereby suggesting that the observed structural effects on AIS formation triggered by EE are mediated by a neuronal activation-dependent mechanism. In agreement, similar morphological differences were observed between cfos$^+$ and cfos$^-$ newborn DGCs in CH animals. In this regard, changes in neuronal activation have been observed to modify AIS structure in diverse experimental paradigms (Grubb and Burrone, 2010; Kuba, 2010, 2012, 2014; Grubb et al., 2011; Evans et al., 2015; Hamada et al., 2016; Yamada and Kuba, 2016).

Conversely, neuroinflammation is a major negative regulator of DGC maturation (Monje et al., 2003). Although we did not observe selective changes in newborn DGC activation in LPS-treated animals, a marked reduction in the nuclear expression of cfos was observed in the general population of DGCs. It can be hypothesized that a reduction in the activity of local networks might slow down the maturation of newborn DGCs, although other relevant mechanisms should also be taken into account. Of note, LPS increased the number and activation of microglial cells in the H, where the newly formed axons of these cells are primarily located. In this regard, microglial cells critically regulate the maturation and integrity of the AIS of principal cortical and hippocampal neurons (Baalman et al., 2015; Benusa et al., 2017). We therefore propose that the putative alteration in the interaction between activated microglial cells in the aforementioned regions and nascent axons harnesses the maturation and development of the AIS in newborn DGCs exposed to LPS.

In conclusion, our data evidence remarkable structural changes in the AIS of newborn DGCs during their maturation under physiological conditions. Moreover, we show that both stimulatory and detrimental effects can alter the dynamics of AIS formation in these cells. On the basis of our findings, we propose that both intrinsic and extrinsic mechanisms drive the formation and structural dynamics of the AIS in newborn DGCs and that these changes in AIS structure are related to alterations in the morphology and functionality of these cells.

References

Alshammari MA, Alshammari TK, Laezza F (2016) Improved methods for fluorescence microscopy detection of macromolecules at the axon initial segment. Front Cell Neurosci 10:5. CrossRef Medline

Altman J, Das GD (1965) Autoradiographic and histological evidence of postnatal hippocampal neurogenesis in rats. J Comp Neurol 124:319–335. CrossRef Medline

Alvarez DD, Giacomini D, Yang SM, Trinchero MF, Temprana SG, Büttner KA, Beltramone N, Schinder AF (2016) A disynaptic feedback network activated by experience promotes the integration of new granule cells. Science 354:459–465. CrossRef Medline

Baalman K, Marin MA, Ho TS, Godoy M, Cherian L, Robertson C, Rasband MN (2015) Axon initial segment-associated microglia. J Neurosci 35:2283–2292. CrossRef Medline

Bender KJ, Trussell LO (2009) Axon initial segment Ca^{2+} channels influence action potential generation and timing. Neuron 61:259–271. CrossRef Medline

Benusa SD, George NM, Sword BA, DeVries GH, Dupree JL (2017) Acute neuroinflammation induces AIS structural plasticity in a NOX2-dependent manner. J Neuroinflammation 14:116. CrossRef Medline

Bergami M, Masserdotti G, Temprana SG, Motori E, Eriksson TM, Göbel J, Yang SM, Conzelmann KK, Schinder AF, Götz M, Berninger B (2015) A critical period for experience-dependent remodeling of adult-born neuron connectivity. Neuron 85:710–717. CrossRef Medline

Bolós M, Pallas-Bazarra N, Terreros-Roncal J, Perea JR, Jurado-Arjona J, Ávila J, Llorens-Martín M (2017) Soluble tau has devastating effects on the structural plasticity of hippocampal granule neurons. Transl Psychiatry 7:1267. CrossRef Medline

Christie SB, De Blas AL (2003) GABAergic and glutamatergic axons innervate the axon initial segment and organize GABA(A) receptor clusters of cultured hippocampal pyramidal cells. J Comp Neurol 456:361–374. CrossRef Medline

Clark KC, Josephson A, Benusa SD, Hartley RK, Baer M, Thummala S, Joslyn M, Sword BA, Elford H, Oh U, Dilsizoglu-Senol A, Lubetzki C, Davenne M, DeVries GH, Dupree JL (2016) Compromised axon initial segment integrity in EAE is preceded by microglial reactivity and contact. Glia 64:1190–1209. CrossRef Medline

Clark K, Sword BA, Dupree JL (2017) Oxidative stress induces disruption of the axon initial segment. ASN Neuro 9:1759091417745426. CrossRef Medline

Colbert CM, Johnston D (1996) Axonal action-potential initiation and Na^+ channel densities in the soma and axon initial segment of subicular pyramidal neurons. J Neurosci 16:6676–6686. CrossRef Medline

Conradi S (1966) Ultrastructural specialization of the initial axon segment of cat lumbar motoneurons. preliminary observations. Acta Soc Med Ups 71:281–284. Medline

Conradi S, Ronnevi LO (1977) Ultrastructure and synaptology of the initial axon segment of cat spinal motoneurons during early postnatal development. J Neurocytol 6:195–210. CrossRef Medline

Dotti CG, Simons K (1990) Polarized sorting of viral glycoproteins to the axon and dendrites of hippocampal neurons in culture. Cell 62:63–72. CrossRef Medline

Edwards SL, Yu SC, Hoover CM, Phillips BC, Richmond JE, Miller KG (2013) An organelle gatekeeper function for *Caenorhabditis elegans* UNC-16 (JIP3) at the axon initial segment. Genetics 194:143–161. CrossRef Medline

Ekdahl CT, Claasen JH, Bonde S, Kokaia Z, Lindvall O (2003) Inflammation is detrimental for neurogenesis in adult brain. Proc Natl Acad Sci U S A 100:13632–13637. CrossRef Medline

Enikolopov G, Overstreet-Wadiche L, Ge S (2015) Viral and transgenic reporters and genetic analysis of adult neurogenesis. Cold Spring Harb Perspect Biol 7:a018804. CrossRef Medline

Evans MD, Dumitrescu AS, Kruijssen DL, Taylor SE, Grubb MS (2015) Rapid modulation of axon initial segment length influences repetitive spike firing. Cell Rep 13:1233–1245. CrossRef Medline

Galiano MR, Jha S, Ho TS, Zhang C, Ogawa Y, Chang KJ, Stankewich MC, Mohler PJ, Rasband MN (2012) A distal axonal cytoskeleton forms an intra-axonal boundary that controls axon initial segment assembly. Cell 149:1125–1139. CrossRef Medline

Gomez-Nicola D, Riecken K, Fehse B, Perry VH (2014) In-vivo RGB marking and multicolour single-cell tracking in the adult brain. Sci Rep 4:7520. CrossRef Medline

González-Cabrera C, Meza R, Ulloa L, Merino-Sepúlveda P, Luco V, Sanhueza A, Oñate-Ponce A, Bolam JP, Henny P (2017) Characterization of the axon initial segment of mice substantia nigra dopaminergic neurons. J Comp Neurol 525:3529–3542. CrossRef Medline

Grubb MS, Burrone J (2010) Activity-dependent relocation of the axon initial segment fine-tunes neuronal excitability. Nature 465:1070–1074. CrossRef Medline

Grubb MS, Shu Y, Kuba H, Rasband MN, Wimmer VC, Bender KJ (2011) Short- and long-term plasticity at the axon initial segment. J Neurosci 31:16049–16055. CrossRef Medline

Gulledge AT, Bravo JJ (2016) Neuron morphology influences axon initial segment plasticity. eNeuro 3:ENEURO.0085–15.2016. CrossRef Medline

Gutzmann A, Ergül N, Grossmann R, Schultz C, Wahle P, Engelhardt M (2014) A period of structural plasticity at the axon initial segment in developing visual cortex. Front Neuroanat 8:11. CrossRef Medline

Hamada MS, Goethals S, de Vries SI, Brette R, Kole MH (2016) Covariation of axon initial segment location and dendritic tree normalizes the somatic action potential. Proc Natl Acad Sci U S A 113:14841–14846. CrossRef Medline

Hedstrom KL, Xu X, Ogawa Y, Frischknecht R, Seidenbecher CI, Shrager P, Rasband MN (2007) Neurofascin assembles a specialized extracellular matrix at the axon initial segment. J Cell Biol 178:875–886. CrossRef Medline

Hu W, Tian C, Li T, Yang M, Hou H, Shu Y (2009) Distinct contributions of Na(v)1.6 and Na(v)1.2 in action potential initiation and backpropagation. Nat Neurosci 12:996–1002. CrossRef Medline

Jones SL, Svitkina TM (2016) Axon initial segment cytoskeleton: architecture, development, and role in neuron polarity. Neural Plast 2016:6808293. CrossRef Medline

Kempermann G, Kuhn HG, Gage FH (1997) More hippocampal neurons in adult mice living in an enriched environment. Nature 386:493–495. CrossRef Medline

Kole MH, Stuart GJ (2012) Signal processing in the axon initial segment. Neuron 73:235–247. CrossRef Medline

Kole MH, Letzkus JJ, Stuart GJ (2007) Axon initial segment Kv1 channels control axonal action potential waveform and synaptic efficacy. Neuron 55:633–647. CrossRef Medline

Kole MH, Ilschner SU, Kampa BM, Williams SR, Ruben PC, Stuart GJ (2008) Action potential generation requires a high sodium channel density in the axon initial segment. Nat Neurosci 11:178–186. CrossRef Medline

Koontz MA (1993) GABA-immunoreactive profiles provide synaptic input

to the soma, axon hillock, and axon initial segment of ganglion cells in primate retina. Vision Res 33:2629–2636. CrossRef Medline
Kuba H (2010) Plasticity at the axon initial segment. Commun Integr Biol 3:597–598. CrossRef Medline
Kuba H (2012) Structural tuning and plasticity of the axon initial segment in auditory neurons. J Physiol 590:5571–5579. CrossRef Medline
Kuba H, Oichi Y, Ohmori H (2010) Presynaptic activity regulates Na(+) channel distribution at the axon initial segment. Nature 465:1075–1078. CrossRef Medline
Kuba H, Adachi R, Ohmori H (2014) Activity-dependent and activity-independent development of the axon initial segment. J Neurosci 34: 3443–3453. CrossRef Medline
Leterrier C (2016) The axon initial segment, 50 years later: a nexus for neuronal organization and function. Curr Top Membr 77:185–233. CrossRef Medline
Leterrier C (2018) The axon initial segment: an updated viewpoint. J Neurosci 38:2135–2145. CrossRef Medline
Leterrier C, Clerc N, Rueda-Boroni F, Montersino A, Dargent B, Castets F (2017) Ankyrin G membrane partners drive the establishment and maintenance of the axon initial segment. Front Cell Neurosci 11:6. CrossRef Medline
Llorens-Martín M, Torres-Alemán I, Trejo JL (2006) Pronounced individual variation in the response to the stimulatory action of exercise on immature hippocampal neurons. Hippocampus 16:480–490. CrossRef Medline
Llorens-Martín M, Tejeda GS, Trejo JL (2010) Differential regulation of the variations induced by environmental richness in adult neurogenesis as a function of time: a dual birthdating analysis. PLoS One 5:e12188. CrossRef Medline
Llorens-Martín M, Fuster-Matanzo A, Teixeira CM, Jurado-Arjona J, Ulloa F, Defelipe J, Rábano A, Hernández F, Soriano E, Ávila J (2013) GSK-3beta overexpression causes reversible alterations on postsynaptic densities and dendritic morphology of hippocampal granule neurons in vivo. Mol Psychiatry 18:451–460. CrossRef Medline
Llorens-Martín M, Jurado-Arjona J, Fuster-Matanzo A, Hernández F, Rábano A, Ávila J (2014) Peripherally triggered and GSK-3beta-driven brain inflammation differentially skew adult hippocampal neurogenesis, behavioral pattern separation and microglial activation in response to ibuprofen. Transl Psychiatry 4:e463. CrossRef Medline
Llorens-Martín M, Rábano A, Ávila J (2015a) The ever-changing morphology of hippocampal granule neurons in physiology and pathology. Front Neurosci 9:526. CrossRef Medline
Llorens-Martín M, Jurado-Arjona J, Ávila J, Hernández F (2015b) Novel connection between newborn granule neurons and the hippocampal CA2 field. Exp Neurol 263:285–292. CrossRef Medline
Llorens-Martín M, Jurado-Arjona J, Bolós M, Pallas-Bazarra N, Ávila J (2016) Forced swimming sabotages the morphological and synaptic maturation of newborn granule neurons and triggers a unique pro-inflammatory milieu in the hippocampus. Brain Behav Immun 53:242–254. CrossRef Medline
Monje ML, Toda H, Palmer TD (2003) Inflammatory blockade restores adult hippocampal neurogenesis. Science 302:1760–1765. CrossRef Medline
Morgan JI, Curran T (1989) Stimulus-transcription coupling in neurons: role of cellular immediate-early genes. Trends Neurosci 12:459–462. CrossRef Medline
Murphy BL, Danzer SC (2011) Somatic translocation: a novel mechanism of granule cell dendritic dysmorphogenesis and dispersion. J Neurosci 31:2959–2964. CrossRef Medline
Nozari M, Suzuki T, Rosa MG, Yamakawa K, Atapour N (2017) The impact of early environmental interventions on structural plasticity of the axon initial segment in neocortex. Dev Psychobiol 59:39–47. CrossRef Medline
Palay SL, Sotelo C, Peters A, Orkand PM (1968) The axon hillock and the initial segment. J Cell Biol 38:193–201. CrossRef Medline
Pallas-Bazarra N, Jurado-Arjona J, Navarrete M, Esteban JA, Hernández F, Ávila J, Llorens-Martín M (2016) Novel function of tau in regulating the effects of external stimuli on adult hippocampal neurogenesis. EMBO J 35:1417–1436. CrossRef Medline
Pallas-Bazarra N, Kastanauskaite A, Ávila J, DeFelipe J, Llorens-Martín M (2017) GSK-3beta overexpression alters the dendritic spines of developmentally generated granule neurons in the mouse hippocampal dentate gyrus. Front Neuroanat 11:18. CrossRef Medline
Palmer LM, Stuart GJ (2006) Site of action potential initiation in layer 5 pyramidal neurons. J Neurosci 26:1854–1863. CrossRef Medline
Petersen AV, Cotel F, Perrier JF (2017) Plasticity of the axon initial segment: fast and slow processes with multiple functional roles. Neuroscientist 23:364–373. CrossRef Medline
Popović ZB, Thomas JD (2017) Assessing observer variability: a user's guide. Cardiovasc Diagn Ther 7:317–324. CrossRef Medline
Rasband MN (2010) The axon initial segment and the maintenance of neuronal polarity. Nat Rev Neurosci 11:552–562. CrossRef Medline
Rodriguez A, Ehlenberger DB, Dickstein DL, Hof PR, Wearne SL (2008) Automated three-dimensional detection and shape classification of dendritic spines from fluorescence microscopy images. PLoS One 3:e1997. CrossRef Medline
Saha R, Knapp S, Chakraborty D, Horovitz O, Albrecht A, Kriebel M, Kaphzan H, Ehrlich I, Volkmer H, Richter-Levin G (2017) GABAergic synapses at the axon initial segment of basolateral amygdala projection neurons modulate fear extinction. Neuropsychopharmacology 42:473–484. CrossRef Medline
Schafer DP, Jha S, Liu F, Akella T, McCullough LD, Rasband MN (2009) Disruption of the axon initial segment cytoskeleton is a new mechanism for neuronal injury. J Neurosci 29:13242–13254. CrossRef Medline
Schambach A, Mueller D, Galla M, Verstegen MM, Wagemaker G, Loew R, Baum C, Bohne J (2006) Overcoming promoter competition in packaging cells improves production of self-inactivating retroviral vectors. Gene Ther 13:1524–1533. CrossRef Medline
Schlüter A, Del Turco D, Deller T, Gutzmann A, Schultz C, Engelhardt M (2017) Structural plasticity of synaptopodin in the axon initial segment during visual cortex development. Cereb Cortex 27:4662–4675. CrossRef Medline
Somogyi P (1979) An interneurone making synapses specifically on the axon initial segment of pyramidal cells in the cerebral cortex of the cat [proceedings]. J Physiol 296:18P–19P. Medline
Song AH, Wang D, Chen G, Li Y, Luo J, Duan S, Poo MM (2009) A selective filter for cytoplasmic transport at the axon initial segment. Cell 136:1148–1160. CrossRef Medline
Tapia M, Wandosell F, Garrido JJ (2010) Impaired function of HDAC6 slows down axonal growth and interferes with axon initial segment development. PLoS One 5:e12908. CrossRef Medline
Toni N, Laplagne DA, Zhao C, Lombardi G, Ribak CE, Gage FH, Schinder AF (2008) Neurons born in the adult dentate gyrus form functional synapses with target cells. Nat Neurosci 11:901–907. CrossRef Medline
van Praag H, Schinder AF, Christie BR, Toni N, Palmer TD, Gage FH (2002) Functional neurogenesis in the adult hippocampus. Nature 415:1030–1034. CrossRef Medline
Wang X, Hooks BM, Sun QQ (2014) Thorough GABAergic innervation of the entire axon initial segment revealed by an optogenetic 'laserspritzer.' J Physiol 592:4257–4276. CrossRef
Watanabe K, Al-Bassam S, Miyazaki Y, Wandless TJ, Webster P, Arnold DB (2012) Networks of polarized actin filaments in the axon initial segment provide a mechanism for sorting axonal and dendritic proteins. Cell Rep 2:1546–1553. CrossRef Medline
Xu X, Shrager P (2005) Dependence of axon initial segment formation on Na^+ channel expression. J Neurosci Res 79:428–441. CrossRef Medline
Yamada R, Kuba H (2016) Structural and functional plasticity at the axon initial segment. Front Cell Neurosci 10:250. CrossRef Medline
Zhao C, Teng EM, Summers RG Jr, Ming GL, Gage FH (2006) Distinct morphological stages of dentate granule neuron maturation in the adult mouse hippocampus. J Neurosci 26:3–11. CrossRef Medline